



Turning foes to friends: Advanced “*in situ* nanovaccine” with dual immunoregulation for enhanced immunotherapy of metastatic triple-negative breast cancer

Ze Wang^{a,1}, Tong Sha^{b,c,1}, Jinwei Li^{b,c}, Huanyu Luo^{b,c}, Annan Liu^a, Hao Liang^a, Jinbiao Qiang^{b,c}, Lei Li^d, Andrew K. Whittaker^e, Bai Yang^a, Hongchen Sun^{b,c}, Ce Shi^{b,c,**}, Quan Lin^{a,*}

^a State Key Laboratory of Supramolecular Structure and Materials, College of Chemistry, Jilin University, Changchun, 130012, PR China

^b Department of Oral Pathology, Hospital of Stomatology, Jilin University, Changchun, 130021, PR China

^c Jilin Provincial Key Laboratory of Science and Technology for Stomatology Nanoengineering, Changchun, 130021, PR China

^d Department of Endocrinology, Lequn Branch, The First Hospital of Jilin University, 130021, PR China

^e Australian Institute for Bioengineering and Nanotechnology, The University of Queensland, Brisbane, QLD, 4072, Australia

ARTICLE INFO

Keywords:

Metastatic triple-negative breast cancer
In situ nanovaccine
Immunogenic cell death
Dual immunoregulation
Synergistic therapy

ABSTRACT

As a “cold tumor”, triple-negative breast cancer (TNBC) exhibits limited responsiveness to current immunotherapy. How to enhance the immunogenicity and reverse the immunosuppressive microenvironment of TNBC remain a formidable challenge. Herein, an “*in situ* nanovaccine” Au/CuNDs-R848 was designed for imaging-guided photothermal therapy (PTT)/chemodynamic therapy (CDT) synergistic therapy to trigger dual immunoregulatory effects on TNBC. On the one hand, Au/CuNDs-R848 served as a promising photothermal agent and nanozyme, achieving PTT and photothermal-enhanced CDT against the primary tumor of TNBC. Meanwhile, the released antigens and damage-associated molecular patterns (DAMPs) promoted the maturation of dendritic cells (DCs) and facilitated the infiltration of T lymphocytes. Thus, Au/CuNDs-R848 played a role as an “*in situ* nanovaccine” to enhance the immunogenicity of TNBC by inducing immunogenic cell death (ICD). On the other hand, the nanovaccine suppressed the myeloid-derived suppressor cells (MDSCs), thereby reversing the immunosuppressive microenvironment. Through the dual immunoregulation, “cold tumor” was transformed into a “hot tumor”, not only implementing a “turning foes to friends” therapeutic strategy but also enhancing immunotherapy against metastatic TNBC. Furthermore, Au/CuNDs-R848 acted as an excellent nanoprobe, enabling high-resolution near-infrared fluorescence and computed tomography imaging for precise visualization of TNBC. This feature offers potential applications in clinical cancer detection and surgical guidance. Collectively, this work provides an effective strategy for enhancing immune response and offers novel insights into the potential clinical applications for tumor immunotherapy.

1. Introduction

Triple-negative breast cancer (TNBC) is a highly aggressive and metastatic cancer, characterized by increased recurrence and mortality rates [1,2]. The efficacy of mainstay treatment options, such as chemotherapy and surgical excision, is often limited due to chemotherapy resistance and other significant side effects. When TNBC

metastasizes to the lungs, bones, or brain, there is little effective therapy [3]. Disturbingly, nearly 46% of TNBC patients metastasize to distant organs within 3 years post-diagnosis. The median survival time of metastatic TNBC patients is only 13.3 months, posing a significant threat to patient health [4]. Inspired by the popular game of “whack-a-mole”, the treatment of both primary and metastatic TNBC requires more than one hammer to impede the compensatory mechanisms of cancer cells

Peer review under responsibility of KeAi Communications Co., Ltd.

* Corresponding author.

** Corresponding author. Department of Oral Pathology, Hospital of Stomatology, Jilin University, Changchun, 130021, PR China.

E-mail addresses: ceshi@jlu.edu.cn (C. Shi), linquan@jlu.edu.cn (Q. Lin).

¹ These authors contributed equally to this work.

<https://doi.org/10.1016/j.bioactmat.2024.04.023>

Received 19 February 2024; Received in revised form 21 April 2024; Accepted 21 April 2024

2452-199X/© 2024 The Authors. Publishing services by Elsevier B.V. on behalf of KeAi Communications Co. Ltd. This is an open access article under the CC BY-NC-ND license (<http://creativecommons.org/licenses/by-nc-nd/4.0/>).

[5]. Concurrently, existing single-mode diagnostic techniques, such as magnetic resonance imaging (MRI) or molybdenum target tube radiographs, has limitations in accurately determining tumor boundaries during surgery. Meanwhile, it is difficult to address issues such as sensitivity, spatial resolution, imaging speed, and complexity. Therefore, there is a pressing need for a multifunctional theranostic integration platform that can effectively diagnose and treat TNBC.

In recent years, there have been rapid developments and breakthroughs in cancer immunotherapy, presenting new opportunities for the prevention and treatment of metastatic tumors. Cancer immunotherapy utilizes the immune system to recognize and eliminate cancer cells through cellular immunology and interactions between the tumors and the host immune system. In this process, tumor-infiltrating lymphocytes (TILs) play a pivotal role. Tumors can be broadly classified as either “cold” or “hot” based on the abundance of TILs [6]. TNBC is typically considered as a “cold tumor” due to the limited presence of activated TILs within the tumor tissue, resulting in immunosuppression and reduced immunogenicity in patients [3,7]. Furthermore, TNBC patients often exhibit an increase in myeloid-derived suppressor cells (MDSCs) that were key components of the immunosuppressive environment [8]. Higher levels of MDSCs are frequently associated with a poor prognosis in TNBC [9]. Consequently, most TNBC patients are resistant to immunotherapy and do not benefit from existing immunotherapeutic approaches. Therefore, reversing this immunosuppressive microenvironment and transforming the tumor into a more immunogenic “hot tumor” represents a significant direction for current TNBC research.

Immunogenic cell death (ICD) is a promising strategy that stimulates immune activation, thereby eliciting effective antitumor immune responses. ICD presents a highly specific approach to managing tumor recurrence and metastasis by provoking the host to generate robust antitumor immune responses. This is achieved through the release of tumor-associated antigens (TAAs) and damage-associated molecular patterns (DAMPs) under the influence of ICD inducers [10–13]. The rapid advancements in nanotechnology and physical chemistry have brought forth numerous novel interventions served as ICD inducers, such as ionizing radiation, photodynamic therapy (PDT), photothermal therapy (PTT), and chemodynamic therapy (CDT) [14,15].

PTT is an emerging tumor treatment modality, and it utilizes photothermal agents to convert near-infrared (NIR) light into heat, thereby achieving thermal ablation of tumors [16–18] and realizing photothermal immunotherapy [19]. Various photothermal agents have been reported, including simulated coordination polyphenol polymers, metal nanoparticles, carbon nanotubes and graphene. Among them, gold nanoparticles (AuNPs) exhibit excellent biocompatibility, optical properties, thermodynamic properties and X-ray attenuation ability. Therefore, AuNPs have been widely used for fluorescence (FL) imaging and computed tomography (CT), as well as PTT of tumors [20,21]. In addition, CDT can catalyze the conversion of endogenous H_2O_2 into reactive oxygen species (ROS) through Fenton or Fenton-like reactions, leading to significant apoptosis of tumor cells by damaging DNA and inactivating proteins [22,23]. Inspired by CDT, researchers have designed nanozymes (nanomaterials with enzyme-like activity) containing transition metal ions (such as Fe^{2+} , Cu^+ , and Mn^{2+}) to induce tumor cell death through Fenton or Fenton-like reactions [24–26]. Moreover, elevated temperatures within the tumor site can enhance the kinetics of the Fenton reaction [27], suggesting that a combination of PTT and CDT may be a promising treatment strategy. This synergistic therapy strategy has the potential to achieve excellent therapeutic efficacy and effectively induce ICD. In the process of ICD, it is possible to construct a personalized cancer vaccine successfully without the need to identify and isolate neoantigens [28,29]. Furthermore, to establish more rapid, potent and durable immune responses with lower therapeutic agent doses, the use of prospective immunoadjuvant is often necessary [30]. Among these adjuvants, toll-like receptor (TLR) agonists, specifically the TLR7/8 agonist resiquimod (R848), have been employed as

immunoadjuvant to the maturation of dendritic cells (DCs) and subsequent expansion of cytotoxic T lymphocytes with the secretion of multiple cytokines [31–34].

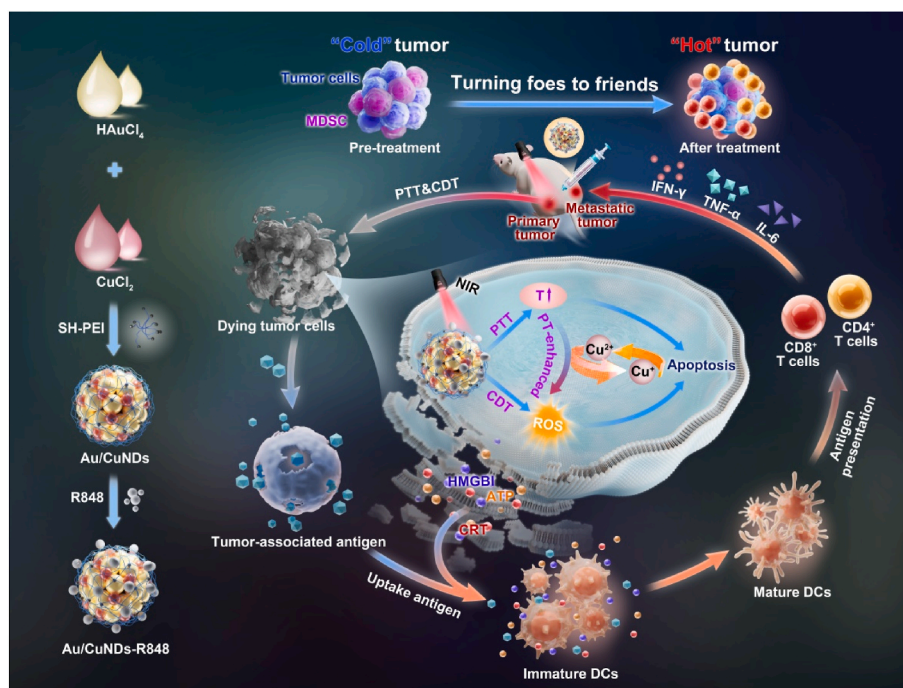
To enhance immunogenicity and reverse the immunosuppressive state of TNBC, we designed an “*in situ* nanovaccine” Au/Cu nanodots-R848 (Au/CuNDs-R848) with dual-mode imaging-guided PTT/CDT synergistic effects (Scheme 1). Firstly, we constructed an excellent photothermal agent and nanozyme Au/CuNDs using a one-step method. Subsequently, the immunoadjuvant R848 was loaded for immune enhancement. Effective PTT and photothermal-enhanced CDT inhibited the progression of primary tumors and made the primary tumor as a source of “individual” TAAs, which was projected to generate intense antigen-specific immunity without invoking ethical concerns associated with traditional tumor vaccines. Meanwhile, DAMPs such as high mobility group box 1 (HMGB1), calreticulin (CRT), and adenosine triphosphate (ATP) were released. With the synergistic assistance of the immunoadjuvant, TAAs and DAMPs were internalized by DCs. Then, DCs underwent the process of maturation and ultimately activated cytotoxic T lymphocytes. Thus, Au/CuNDs-R848 played a role of an “*in situ* nanovaccine” to enhance the immunogenicity of TNBC by inducing ICD. Furthermore, ICD triggered a robust inflammatory response marked by the secretion of interferon- γ (IFN- γ), tumor necrosis factor- α (TNF- α), and interleukin-6 (IL-6), thereby inhibiting the growth of metastatic tumors. Simultaneously, the immunosuppressive MDSCs were effectively inhibited during this process, thereby reversing the immunosuppressive microenvironment. Ultimately, the “cold tumor” transformed into a “hot tumor”, implemented the “turning foes to friends” therapeutic strategy. Overall, Au/CuNDs-R848 as an “*in situ* nanovaccine” with dual immunoregulation enables enhanced immunotherapy against metastatic TNBC. Moreover, Au/CuNDs-R848 served as an excellent nanoprobe, facilitating accurate visualization of TNBC through near-infrared fluorescence imaging and CT imaging, thereby achieving the integration of diagnosis and treatment.

2. Results and discussion

2.1. Synthesis and characterization of Au/CuNDs-R848

An advanced “*in situ* nanovaccine” Au/CuNDs-R848 was designed for imaging-guided PTT and photothermal-enhanced CDT, which triggered dual immunoregulation to enhance immunotherapy of TNBC. The structure, morphology, and properties of Au/CuNDs-R848 were investigated in detail. In terms of structure, the 1H NMR spectra of Au/CuNDs, R848, and Au/CuNDs-R848 were analyzed. As shown in Fig. 1a, after the combination of Au/CuNDs with R848, the peaks of R848 at 7.71 ppm and 4.99 ppm shifted to the high field area (7.64 ppm and 4.95 ppm, respectively). This indicated that the H atoms of the aromatic ring and amidogen on R848 interact with the Au/CuNDs, resulting in a change in the chemical shift. We further analyzed the infrared spectra of Au/CuNDs, R848, and Au/CuNDs-R848 (Fig. 1b). After connecting R848, Au/CuNDs-R848 exhibited characteristic peaks at 3000 and 2900 cm^{-1} (hydroxyl stretching vibration), 1210 and 1310 cm^{-1} (C–O bond stretching vibration), 780 and 708 cm^{-1} (benzene), which further indicated the successful connection between the two. The zeta potential was investigated. Since PEI was selected as the ligand, the synthesized Au/CuNDs exhibited a large positive charge ($+10.28 \pm 0.44$ mV). The zeta potential of Au/CuNDs-R848 ($+6.59 \pm 0.48$ mV) decreased slightly after the supramolecular interaction between Au/CuNDs and R848 (Fig. 1c). All of these results support the formation of a stable structure of Au/CuNDs-R848.

The morphology of Au/CuNDs and Au/CuNDs-R848 was investigated by transmission electron microscope (TEM). TEM images showed that the Au/CuNDs were monodisperse, with a distinct spherical shape and an average size of about 2.0 nm (Fig. S1 and Fig. S2). After connecting with R848, the Au/CuNDs-R848 still maintained a good spherical shape, and the size increased slightly, with an average size of



Scheme 1. An advanced “*in situ* nanovaccine” Au/CuNDs-R848 for dual-mode imaging and photothermal-chemodynamic therapy, which triggered dual immunoregulation to enhance immunotherapy against metastatic triple-negative breast cancer.

approximately 2.4 nm (Fig. 1d and e). The UV absorption spectrum of Au/CuNDs-R848 was investigated. As shown in Fig. 1f, Au/CuNDs-R848 exhibited a broad absorption band within the tested range. The solution of Au/CuNDs-R848 appeared brown (Fig. 1f).

To further determine the elemental composition and valence states of Au/CuNDs-R848, X-ray photoelectron spectroscopy (XPS) was used. As shown in Fig. 1g, the XPS spectrum revealed the typical signals for Au, Cu, and S. The peaks at 87.7 and 84.0 eV were assigned to Au 4f_{5/2} and Au 4f_{7/2}, respectively, indicating the presence of both Au (0) and Au (I) in the Au/CuNDs-R848 [35,36] (Fig. 1h). Au (0) contributes to the nucleation of nanodots, while Au (I) forms stable Au–S bonds with ligands, improving the stability of nanodots and endowing them with bright and stable fluorescence characteristics. The Cu 2p peaks at 932.2 and 952.1 eV were assigned to Cu⁺, and the peaks at 932.7 and 954.0 eV were associated with Cu²⁺ (Fig. 1i) [27], suggesting the potential for Fenton reaction-based chemodynamic therapy (CDT).

2.2. Photothermal performance

PTT is a burgeoning treatment method that employs photothermal agents to convert near-infrared light into heat, resulting in the thermal ablation of tumors. Among various photothermal agents, gold-based nanomaterials exhibit excellent thermodynamic properties, making them highly promising candidates for effective PTT. We investigated the photothermal performance of Au/CuNDs-R848. As displayed in the photothermal heating curves (Fig. 2a), the corresponding temperature elevation (ΔT) of Au/CuNDs-R848 increased by 20.1 °C after 10 min of 808 nm laser irradiation at a power density of 2.0 W/cm². In contrast, the PBS solution showed a negligible increase in temperature ($\Delta T = 4.9$ °C) under identical conditions. The difference in temperature between Au/CuNDs-R848 and PBS can be further visualized in the thermal imaging pictures (Fig. 2b). In addition, the temperature increase of Au/CuNDs-R848 at different power densities was tested. The Au/CuNDs-R848 solution was subjected to an 808 nm laser at power densities ranging from 1.0 to 2.5 W/cm² for 10 min. As illustrated in Fig. 2c, the ΔT of Au/CuNDs-R848 increased with higher laser power, demonstrating a laser power-dependent photothermal effect. The stability of

the photothermal agents also holds significant importance. The temperature of Au/CuNDs-R848 remained relatively stable after four consecutive laser on/off cycles, suggesting excellent photothermal stability (Fig. 2d). The above results indicated that Au/CuNDs-R848 held substantial potential for application as photothermal agents.

2.3. Enhanced CDT performance

Fenton reaction-based chemodynamic therapy (CDT) is an emerging nano-catalytic therapy that can convert H₂O₂ to ROS, consequently inducing oxidative stress in cancer cells. Moreover, increasing the temperature can expedite the kinetics of Fenton reaction, which suggests that PTT and CDT synergistic therapy could be a promising therapeutic strategy and effectively induce ICD.

Recently, Cu-based catalysts have garnered interest due to their adaptability to a broad pH range, high reaction rate, and cost-effectiveness [37]. In this study, the methylene blue (MB) probe was used to evaluate the catalase-like activity of Au/CuNDs-R848 in producing ·OH radicals through Fenton-like reaction. Firstly, we examined the generation of ·OH radicals by Au/CuNDs-R848 in the presence of H₂O₂. As shown in Fig. S3, the MB absorbance was consistently decreased with increasing H₂O₂ concentration, accompanied by a gradual increase in ·OH radical produced by Au/CuNDs-R848, revealing a concentration-dependent relationship with H₂O₂. The results demonstrated the excellent ability of Au/CuNDs-R848 to catalyze Fenton-like reaction. Then, the effect of different pH levels on the efficiency of Fenton reaction was investigated. A decline in MB absorbance at low pH values indicated the generation of a larger quantity of ·OH radicals (Fig. 2e). This indicated that Au/CuNDs-R848 can proficiently induce ·OH generation by decomposing H₂O₂ under acidic conditions, and the slightly mildly acidic tumor environment of the tumor was conducive to the occurrence of the Fenton reaction.

Importantly, the efficiency of the Fenton reaction is closely associated with the reaction temperature. The exemplary photothermal properties of Au/CuNDs-R848 prompted us to explore the potential of NIR laser mediated photo-assisted Fenton reaction. Therefore, the enzymatic activity of Au/CuNDs-R848 under different laser power

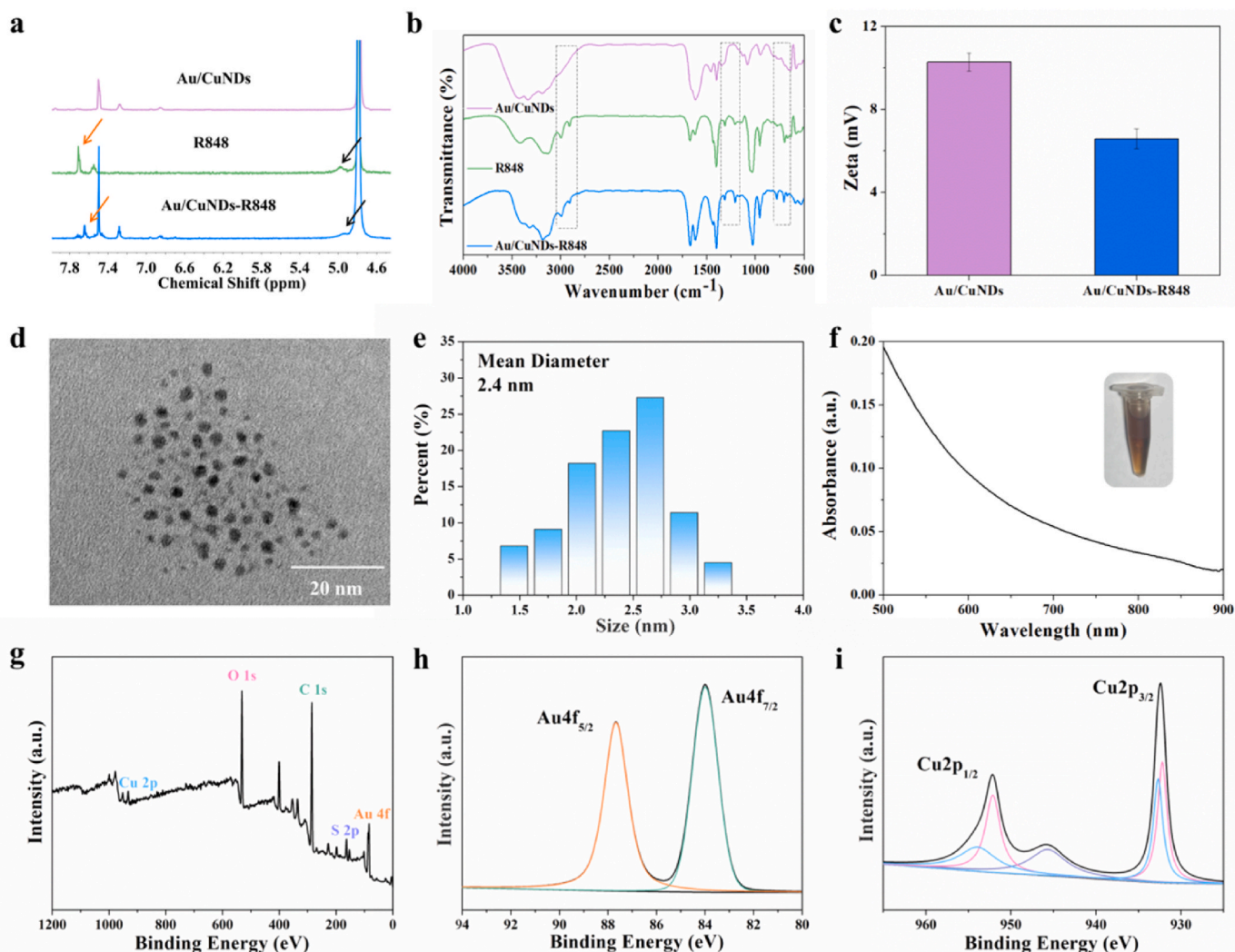


Fig. 1. Structure, morphology, and composition characterization of Au/CuNDs-R848. (a) ^1H NMR spectrum and (b) FTIR spectra of Au/CuNDs, R848, and Au/CuNDs-R848. (c) Zeta potential of Au/CuNDs and Au/CuNDs-R848. (d) TEM image and (e) size distribution histogram of the Au/CuNDs-R848. (f) UV-vis absorption spectrum of Au/CuNDs-R848. Inset, photographs of Au/CuNDs-R848 solution. (g) XPS survey spectrum of Au/CuNDs-R848. High-resolution XPS spectra of (h) Au 4f and (i) Cu 2p of Au/CuNDs-R848.

densities (0.5, 1.0, 1.5, 2.0 W/cm^2) in the presence of H_2O_2 was evaluated. As shown in Fig. 2f, with the increase of power density, the absorbance of MB decreases, indicating that the amount of $\cdot\text{OH}$ radicals produced is greatly increased. Subsequently, 5,5'-dimethylpyrroline-1-oxide (DMPO) was used as a spin trap agent to detect $\cdot\text{OH}$ generation via electron spin resonance (ESR). Fig. 2g displays an intense $\cdot\text{OH}$ signal produced by Au/CuNDs-R848 upon 808 nm laser irradiation, indicating that high temperature improves catalytic efficiency of Au/CuNDs-R848. These results collectively demonstrate that a temperature rise effectively augments the production of $\cdot\text{OH}$ radicals by Au/CuNDs-R848, thereby achieving photothermal-enhanced CDT.

Depleting intratumoral glutathione (GSH) can improve the efficacy of CDT [26]. GSH is an intracellular antioxidant that can scavenge $\cdot\text{OH}$ produced by the Fenton reaction. XPS spectrogram analysis revealed the presence of Cu^{2+} on the surface of Au/CuNDs-R848, indicating that it has the potential to consume GSH. We examined the GSH depletion capacity of Au/CuNDs-R848 using 5,5'-dithiobis-(2-nitrobenzoic acid) (DTNB). As shown in Fig. 2h, GSH was gradually consumed by Au/CuNDs-R848 with the increase of reaction time. In addition, acidic conditions further enhance GSH depletion, signifying that Au/CuNDs-R848 possesses superior GSH consumption capabilities (Fig. S4). In summary, Au/CuNDs-R848 has the potential to interact

with excess GSH, leading to the generation of Cu^+ and oxidized glutathione (GSSG) within the tumor microenvironment. The depletion of GSH not only mitigates ROS scavenging but also enhances the Fenton reaction through the utilization of the generated Cu^+ , which is beneficial for subsequent CDT.

2.4. NIR-II fluorescence and CT imaging performance in vitro

Recent advancements in second near-infrared (NIR-II, 1000–1700 nm) fluorescence imaging have garnered significant attention due to their superior tissue penetration, high signal-to-noise ratio, and reduced background autofluorescence. It is of clinical significance to develop a NIR-II fluorescent probe with long wavelength, high brightness, excellent stability and biocompatibility. Therefore, we designed the Au/CuNDs-R848 fluorescence probe with excellent NIR-II fluorescence imaging capabilities, and proceeded to assess its *in vitro* imaging performance.

Firstly, we characterized the fluorescence spectrum of Au/CuNDs-R848. Au/CuNDs-R848 had a strong emission peak at 1073 nm, and the emission tail extends to 1300 nm, with almost all of the emission spectrum falling in the NIR-II region (Fig. 3a). To highlight the clinical application potential of the prepared Au/CuNDs-R848 fluorescent

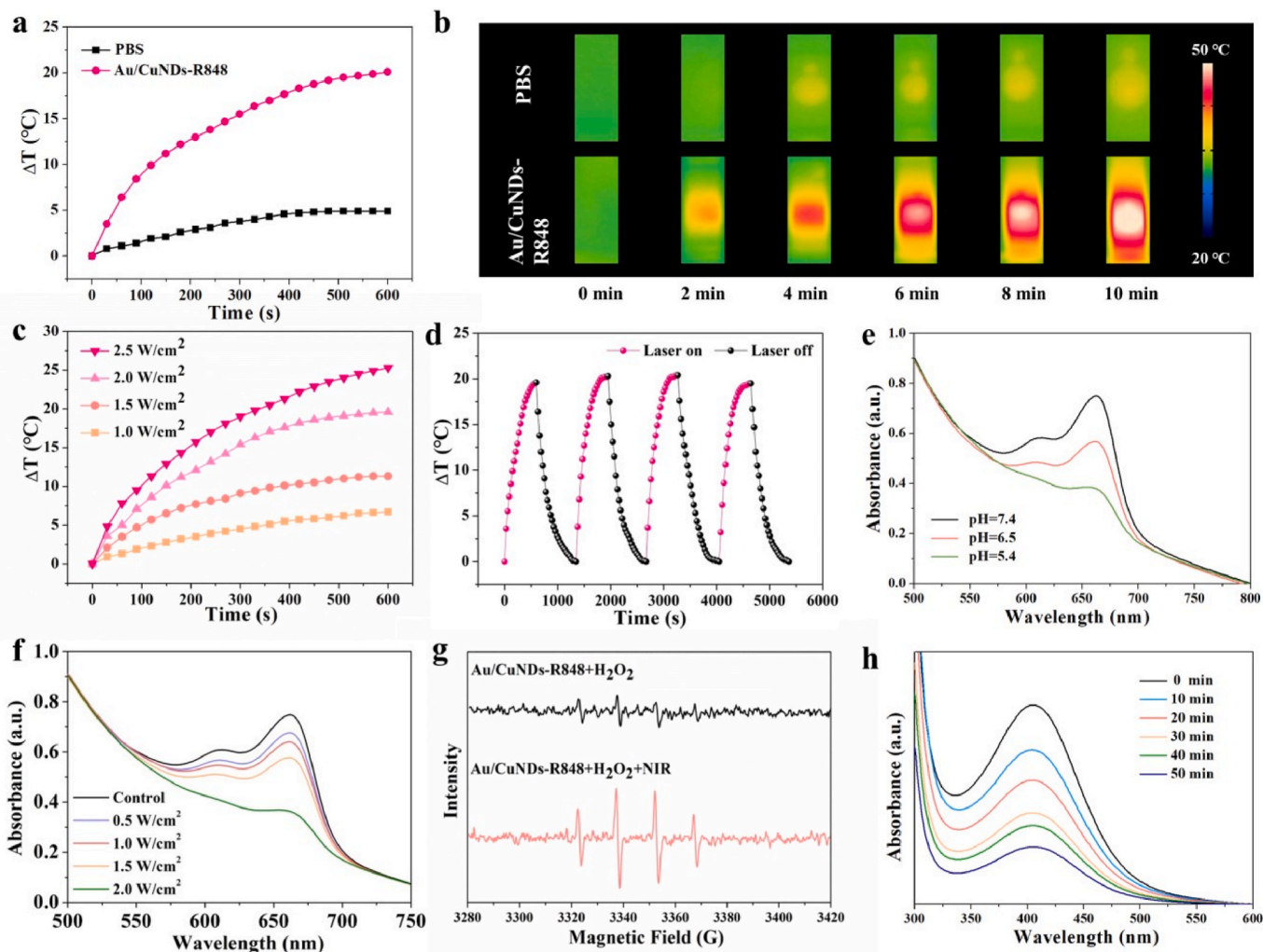


Fig. 2. Evaluation of the photothermal and chemodynamic properties of Au/CuNDS-R848. (a) Temperature elevation and (b) infrared thermal images of PBS (used as control) and Au/CuNDS-R848 under 808 nm laser irradiation as a function of irradiation time. (c) Temperature profiles of Au/CuNDS-R848 under 808 nm laser irradiation at different power densities (1.0, 1.5, 2.0, and 2.5 W/cm²). (d) Thermal stability of Au/CuNDS-R848. (e) Absorbance of MB after the addition of Au/CuNDS-R848 and H₂O₂ at different pH levels (5.4, 6.5, and 7.4). (f) Absorbance of MB after the addition of Au/CuNDS-R848 and H₂O₂ under different laser power irradiations (0.5, 1.0, 1.5, 2.0 W/cm²). (g) ESR spectra under various reaction conditions with DMPO as a spin trap agent. (h) GSH depletion by Au/CuNDS-R848.

probe, clinically approved indocyanine green (ICG) was incorporated for comparison. As can be seen from Fig. 3b and c, Au/CuNDS-R848 outperforms ICG, registering a NIR-II emission intensity approximately 1.3 times higher. The enhanced brightness facilitates NIR-II imaging over the 1000–1400 nm window, minimizing exposure durations, mitigating background interference, and bolstering imaging depth and contrast. Crucially, for *in vivo* applications, photostability is pivotal. Fig. 3b and c depicted the declining fluorescence intensity of ICG upon incremental durations (0, 10, 20, 30, 40, 50 min) of 808 nm laser exposure, indicating obvious photobleaching. Compared with ICG, the fluorescence intensity of the prepared Au/CuNDS-R848 remained stable, demonstrating promising photostability and resistance to photobleaching. Furthermore, as Au/CuNDS-R848 concentration increased, there was a corresponding rise in fluorescence signal intensity, illustrating a robust linear correlation ($R^2 = 0.997$, Fig. 3d). Thus, Au/CuNDS-R848 with superior fluorescence brightness and stability are expected to be a promising fluorescent probe for clinical imaging and diagnostics.

Owing to the excellent X-ray attenuation ability of Au, the synthesized Au/CuNDS-R848 showcased effective CT imaging characteristics. We evaluated the *in vitro* CT imaging attributes to gauge its feasibility as a clinical contrast agent. Fig. 3e revealed that as the concentration of Au/CuNDS-R848 augments, there was a corresponding amplification in

the CT intensity, establishing a robust linear relationship ($R^2 = 0.95$). Therefore, this facilitates the quantitative analysis of the *in vivo* accumulation of Au/CuNDS-R848 based on imaging outcomes.

2.5. PTT/CDT-mediated tumor cell death *in vitro*

Excellent biocompatibility of biomaterials is a fundamental prerequisite for *in vivo* biological applications. Then, we evaluated the biocompatibility of Au/CuNDS-R848 by hemolysis assay and cell counting kit-8 (CCK-8) assay. As shown in Fig. S5, both Au/CuNDS and Au/CuNDS-R848 exhibited negligible hemolysis (<5%) at concentrations up to 400 μg/mL, indicating excellent biocompatibility of Au/CuNDS-R848. To investigate the potential cytotoxic effects, the viability of 4T1 cells (a murine triple-negative breast cancer cell line) and HC11 cells (a murine mammary epithelial cell line) was mensurated after incubation with Au/CuNDS-R848 for 24 h utilizing a CCK-8 assay. HC11 cells exhibited a robust survival rate (>90%) at a concentration of 200 μg/mL. Conversely, 4T1 cells displayed a survival rate of $79.63 \pm 1.65\%$ (Fig. 4a), indicating a specific tumor cell killing effect. The disparity in survival rates between HC11 and 4T1 cells can be attributed to the relatively higher levels of H₂O₂ within 4T1 cells, which enhanced the effectiveness of CDT induced by Au/CuNDS-R848. Based on the

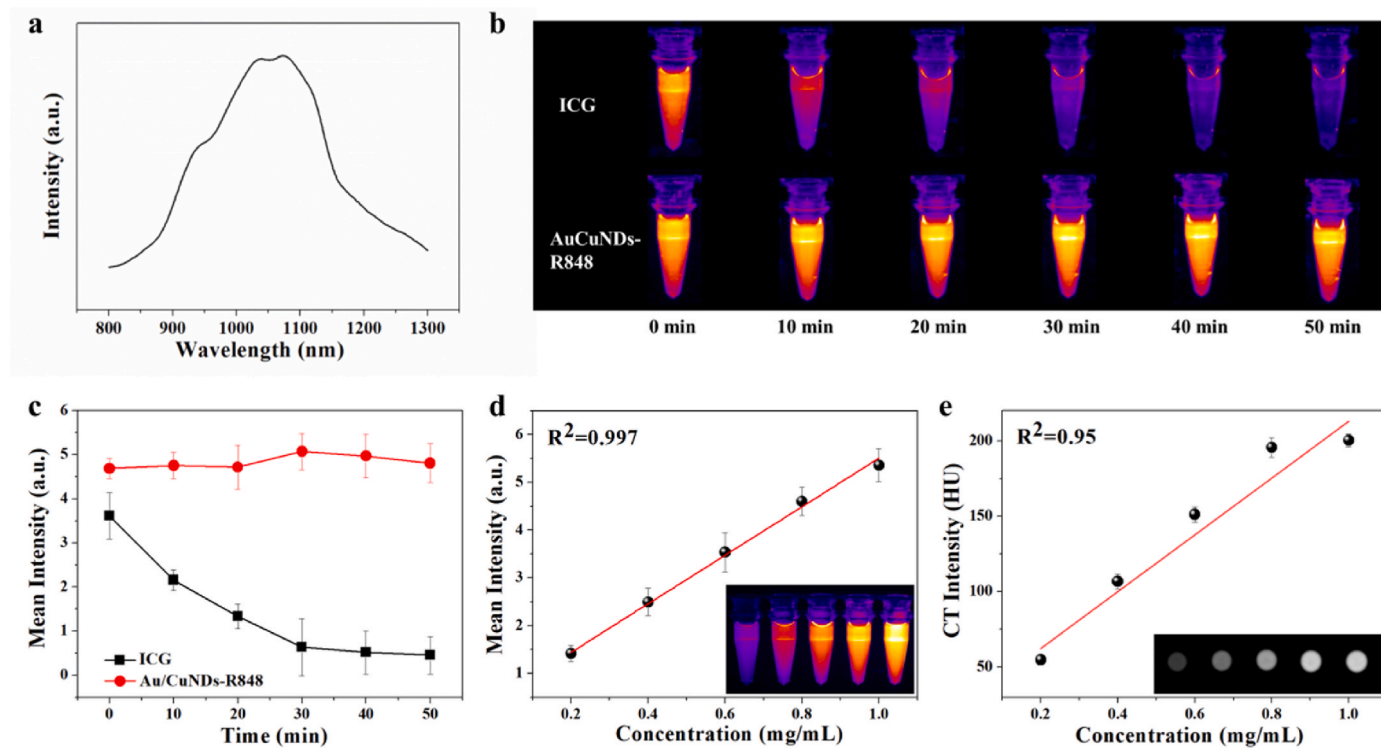


Fig. 3. *In vitro* NIR-II fluorescence and CT imaging properties of Au/CuNDs-R848. (a) Emission spectrum of Au/CuNDs-R848. (b) Photostability and (c) fluorescence intensity of Au/CuNDs-R848 and ICG. Trends in (d) FL intensity and (e) CT intensity of Au/CuNDs-R848 across varying concentrations. Inset, FL images and CT images at specific Au/CuNDs-R848 concentrations.

above findings, a concentration of 200 $\mu\text{g/mL}$ for Au/CuNDs-R848 was selected for subsequent *in vitro* experiments.

Moreover, Au/CuNDs-R848 demonstrated remarkable photothermal properties and a capacity to enhance Fenton reaction-based CDT in conjunction with temperature elevation, thus facilitating increased generation of ROS for cancer cell eradication. We evaluated the synergistic therapeutic effect and intrinsic ROS levels of Au/CuNDs-R848-mediated PTT and photothermal-enhanced CDT *in vitro*. Fig. 4b illustrated a perceptible inhibition in 4T1 cell viability, correlating with the incremental power density during a 5-min laser exposure. At a power density of 2 W/cm^2 , the survival rate of 4T1 cells was approximately $34.17 \pm 1.27\%$. As shown in Fig. 4c and d, the introduction of Au/CuNDs-R848 led to an increase in intracellular ROS production. The increase was significantly amplified when treated with Au/CuNDs-R848+NIR (2 W/cm^2), exhibiting a 3.79-fold increase compared to the control group. The result indicated that Au/CuNDs-R848 can catalyze the Fenton reaction and promote ROS generation in 4T1 cells. Furthermore, the excellent photothermal property of Au/CuNDs-R848 enhanced the catalytic performance. ROS not only induces DNA damage in cancer cells but also promotes oxidative stress in the endoplasmic reticulum, which is crucial for the initiation of immunogenic cell death (ICD) [6]. Based on the above results, a power density of 2 W/cm^2 was chosen as the optimal parameter for laser irradiation in subsequent experiments.

The Live/Dead staining technique was used to assess the efficacy of tumor cell killing. As shown in Fig. S6, 4T1 cells were stained using calcein-AM and propidium iodide (PI) after different treatments. Notably, the Au/CuNDs-R848+NIR group displayed a significantly enhanced PI positivity, underscoring the effectiveness of the PTT and photothermal-enhanced CDT synergistic therapy on 4T1 cells. In addition, flow cytometry was used to further quantify the effect of the treatment on apoptosis (Fig. 4e and f). Compared to the other groups, the apoptosis rates of 4T1 cells treated by Au/CuNDs-R848 in combination with laser irradiation significantly increased and reached $39.5 \pm$

0.7%, indicating an effective synergistic therapeutic effect. These results corroborated that Au/CuNDs-R848-mediated PTT/CDT potently augments 4T1 cells death.

2.6. Induction of ICD *in vitro*

Au/CuNDs-R848-mediated PTT and photothermal-enhanced CDT effectively induced tumor cell death *in vitro*, providing a basis for ICD. Therefore, we explored the ability of Au/CuNDs-R848-mediated PTT/CDT to effectively induce ICD in 4T1 cells. ICD is characterized by the release of DAMPs, which are manifested through the secretion of various substances and the exposure of distinct markers on the cell surface. In the pro-apoptotic stage, cells undergoing ICD translocate CRT to their surface, acting as an “eat me” signal that promotes phagocytosis by DCs [38]. ATP released from cancer cells in the blebbing phase of apoptosis functions as a “find me” signal for dendritic cell precursors [39]. Later in apoptosis, HMGB1 is released from the nuclei of damaged or disrupted cells [40]. In our study, we detected CRT exposure, ATP secretion, and HMGB1 release as indicators of ICD. Fig. 5a and b demonstrated that the Au/CuNDs-R848+NIR group exhibited a significantly higher level of CRT exposure on 4T1 cell surface compared with the control group, suggesting that Au/CuNDs-R848-based synergistic therapy can indeed induce ICD. Moreover, the concentration of ATP increased after treatment with Au/CuNDs+NIR and Au/CuNDs-R848+NIR (Fig. 5c), being 2.1-fold and 2.25-fold higher than the control group, respectively. To detect HMGB1 release, we employed ELISA and CLSM. As shown in Fig. 5d, the nanomaterials alone or laser irradiation alone had a limited effect on inducing the release of HMGB1. However, the treatment with Au/CuNDs-R848 combined with laser irradiation resulted in a significant increase in HMGB1 concentrations in the medium (Fig. 5d) and observable translocation of HMGB1 from the nucleus, as indicated by the arrows in Fig. 5e. All the above results indicated that Au/CuNDs-R848-mediated PTT/CDT can effectively induce CRT exposure, ATP secretion, and HMGB1 release, underscoring the superior

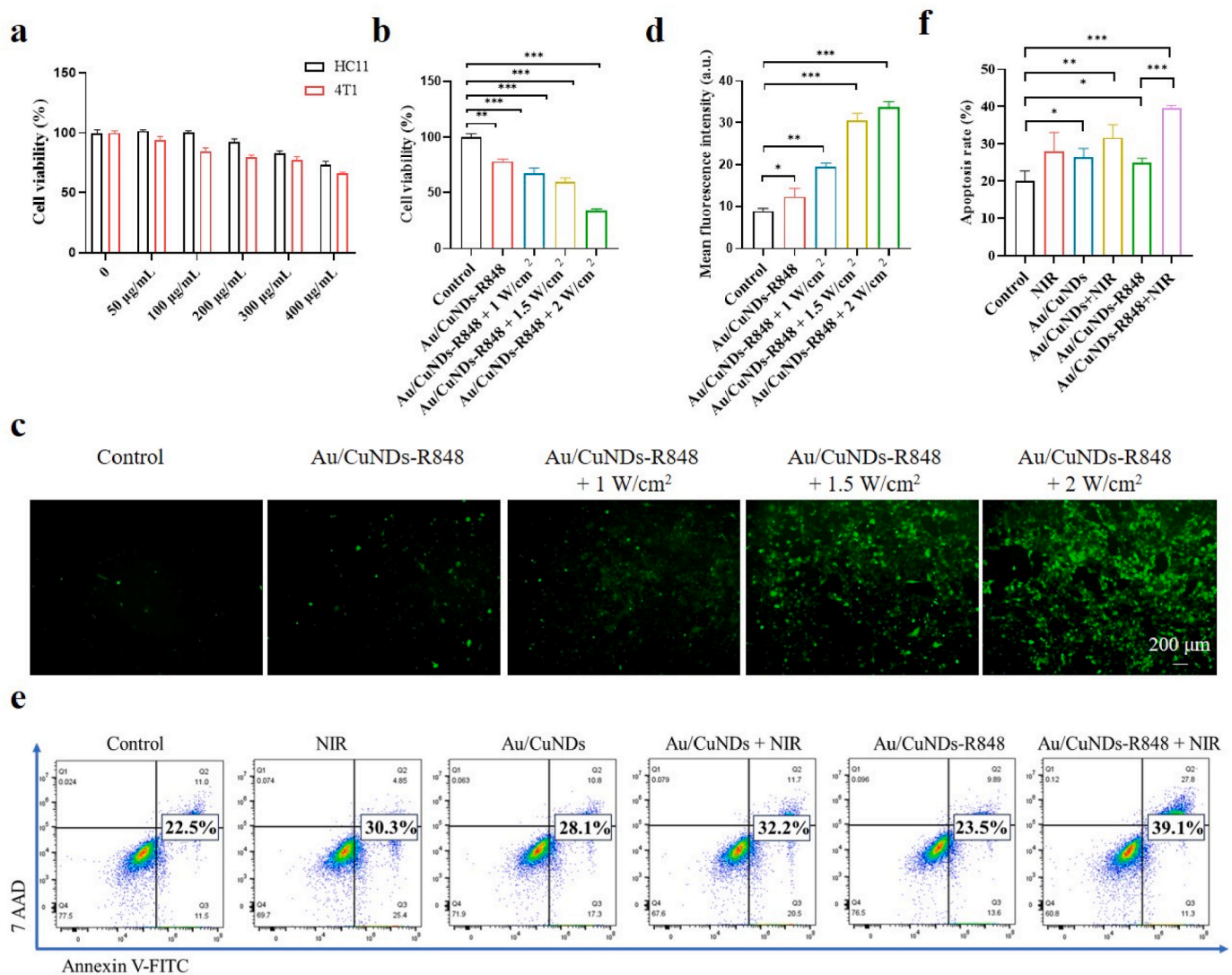


Fig. 4. *In vitro* detection of synergistic therapeutic effects and intracellular ROS. (a) Cell viability of 4T1 and HC11 cells after 24-h exposure to graded concentrations of Au/CuNds-R848 (0, 50, 100, 200, 300, and 400 μg/mL). (b) Cell viability of 4T1 cells after incubation with Au/CuNds-R848 in the absence or presence of 808 nm laser irradiation at different power densities (1.0, 1.5, and 2.0 W/cm²). (c) Fluorescence images displaying ROS levels in 4T1 cells stained with DCFH-DA, subsequent to different treatments (scale bar: 200 μm). (d) Quantification of intracellular ROS levels across different treatments (n = 3). (e) Apoptosis quantification in 4T1 cells treated with Au/CuNds or Au/CuNds-R848, with and without 808 nm laser irradiation at 2.0 W/cm², as analyzed by flow cytometry. (Q2: late apoptotic cells; Q3: early apoptotic cells), with percentages indicating the overall apoptosis rate (Q2 + Q3). (f) Apoptosis rate of 4T1 cells treated with Au/CuNds or Au/CuNds-R848, with and without 808 nm laser irradiation at 2.0 W/cm² *P < 0.05, **P < 0.01, ***P < 0.001.

efficacy of inducing ICD.

Further, we developed an *in vitro* model to evaluate the potential of the released DAMPs in promoting the maturation of DCs (Fig. 5f). Specifically, bone marrow-derived cells were cultured with GM-CSF (20 ng/mL) and IL-4 (20 ng/mL) for 6 days to yield immature bone marrow dendritic cells (BMDCs). Concurrently, 4T1 cells underwent various treatments. Subsequently, the treated 4T1 cells were co-cultured with the immature BMDCs for 24 h. The maturation of BMDCs was analyzed using a gating strategy based on the co-stimulatory molecules CD11c, CD80, and CD86, as illustrated in Fig. 5g. LPS served as a positive control, achieving a maturation rate of BMDCs to approximately 95.8% (Fig. 5g). Notably, the Au/CuNds-R848+NIR group remarkably augmented the maturation of BMDCs in comparison with other groups, which was attributed to the synergistic effects of PTT, CDT, and R848 stimulation (Fig. 5h and Fig. S7). The maturation rate of BMDCs in Au/CuNds-R848+NIR group reached up to 80.6%, which closely approached the maturation level observed in the LPS group among all treatment groups. Therefore, Au/CuNds-R848-mediated PTT/CDT can

effectively induce ICD and promote the maturation of DCs, thereby establishing the foundation for T cell-mediated immune response.

2.7. Dual-mode imaging guided treatment *in vivo*

Molecular imaging techniques such as CT and FL provide essential technical support for accurate detection of tumor localization to avoid damage to healthy tissue in conventional treatments (such as surgical resection, radiotherapy, and PTT). Unfortunately, existing clinical contrast agents primarily offer single-mode imaging, which presents limitations in terms of sensitivity, spatial resolution, imaging speed, and complexity. To address these issues, we designed an excellent nanoprobe Au/CuNds-R848, which possesses superior FL/CT dual-mode imaging capabilities.

Owing to the exceptional NIR-II FL and CT imaging performance of Au/CuNds-R848, the nanoprobe can pinpoint tumor locations, facilitating imaging-guided precision therapy. As demonstrated in Fig. 6a and c, Au/CuNds-R848 displayed more robust NIR-II fluorescence intensity

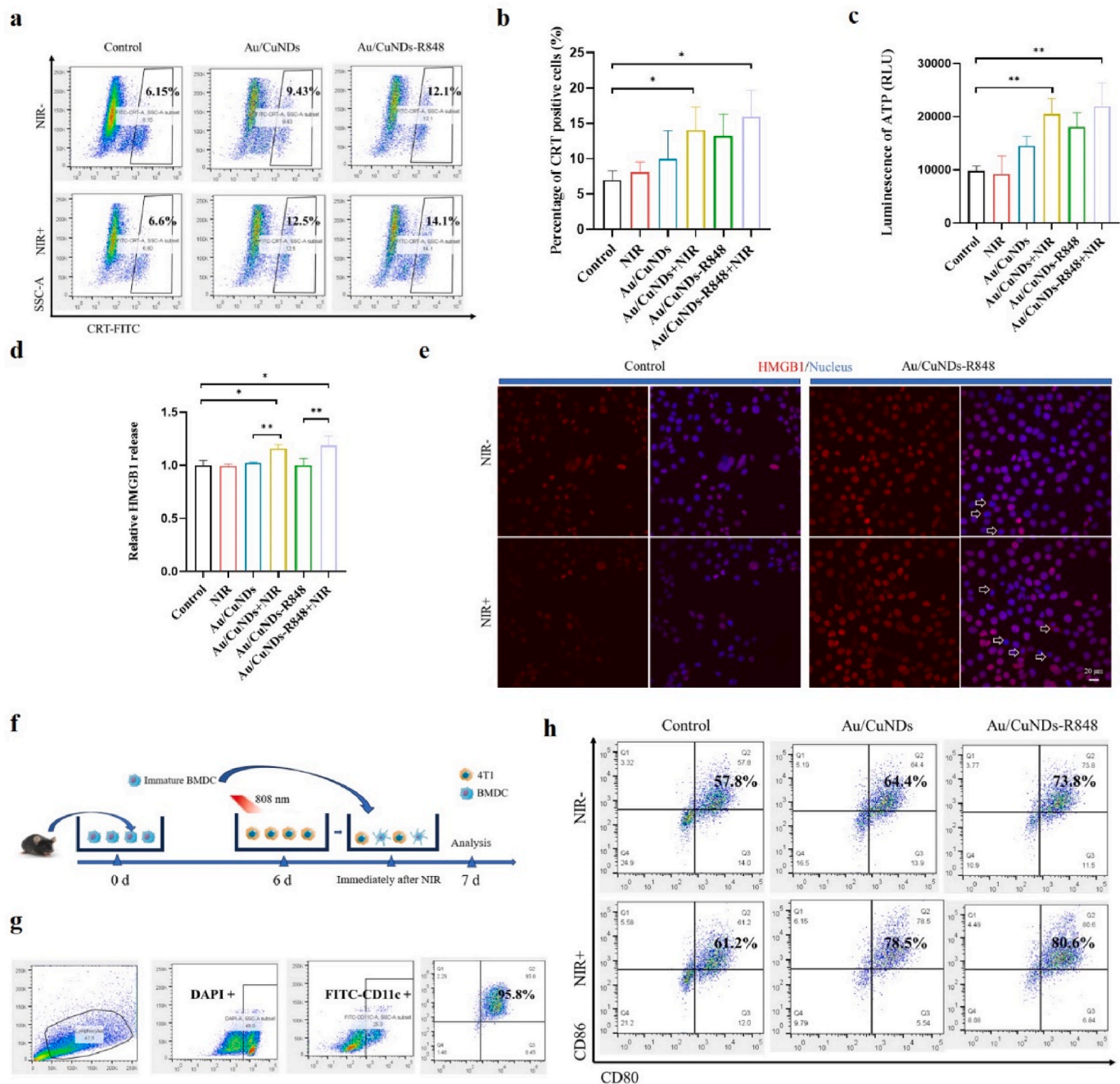


Fig. 5. *In vitro* induction of ICD in tumor cells by Au/CuNDs-R848-mediated PTT/CDT. (a) Cell surface CRT expression was determined by flow cytometry 12 h post-treatment. (b) Quantitative analysis of CRT expression on cell surfaces across different treatment groups ($n = 3$). (c) Detection of extracellular ATP levels in 4T1 cells 2 h after treatment, quantified by luminescence ($n = 3$). (d) Quantification of HMGB1 release into the medium 24 h post-treatment, measured by enzyme-linked immunosorbent assay (ELISA). (e) Translocation of HMGB1 (red) using confocal laser scanning microscope (CLSM), with cell nuclei counterstained with DAPI (blue). (scale bar: 20 μm) (f) Schematic illustration of the *in vitro* maturation of DCs induced by Au/CuNDs-R848. (g) Gating strategy of flow cytometry employed to identify matured DCs based on the expression of co-stimulatory molecules CD11c, CD80, and CD86. (h) Flow cytometry analysis of mature DCs (CD11c^+ , CD80^+ , and CD86^+) in different treatment groups ($n = 3$). * $P < 0.05$, ** $P < 0.01$, *** $P < 0.001$.

in vivo compared to ICG. Notably, the entire tumor can be distinctly visualized, suggesting the potential of Au/CuNDs-R848 for surgical procedures that demand clearer visualization. Fluorescence distribution was also observed in resected organs and tumors among the different groups. Compared with ICG group, the Au/CuNDs-R848 group showed higher luminescence intensity at the tumor site (Fig. S8). Meanwhile, Au/CuNDs-R848 exhibited commendable CT imaging capabilities *in vivo* (Fig. 6b). The CT signal at the tumor site gradually diminished over time (Fig. 6d), consistent with the FL imaging observations. The robust dual-

mode imaging capability of Au/CuNDs-R848 has the potential to enhance diagnostic sensitivity and precision.

Surgery is important for the local management of TNBC at an early stage. Consequently, ensuring surgical precision is of utmost importance. Accurate differentiation between tumor and normal tissue is obligatory to minimize the risk of recurrence and prevent collateral damage to normal tissue. FL imaging-guided surgery has garnered considerable attention in clinical research due to its potential to facilitate precise tumor resection. Unfortunately, the broad application of

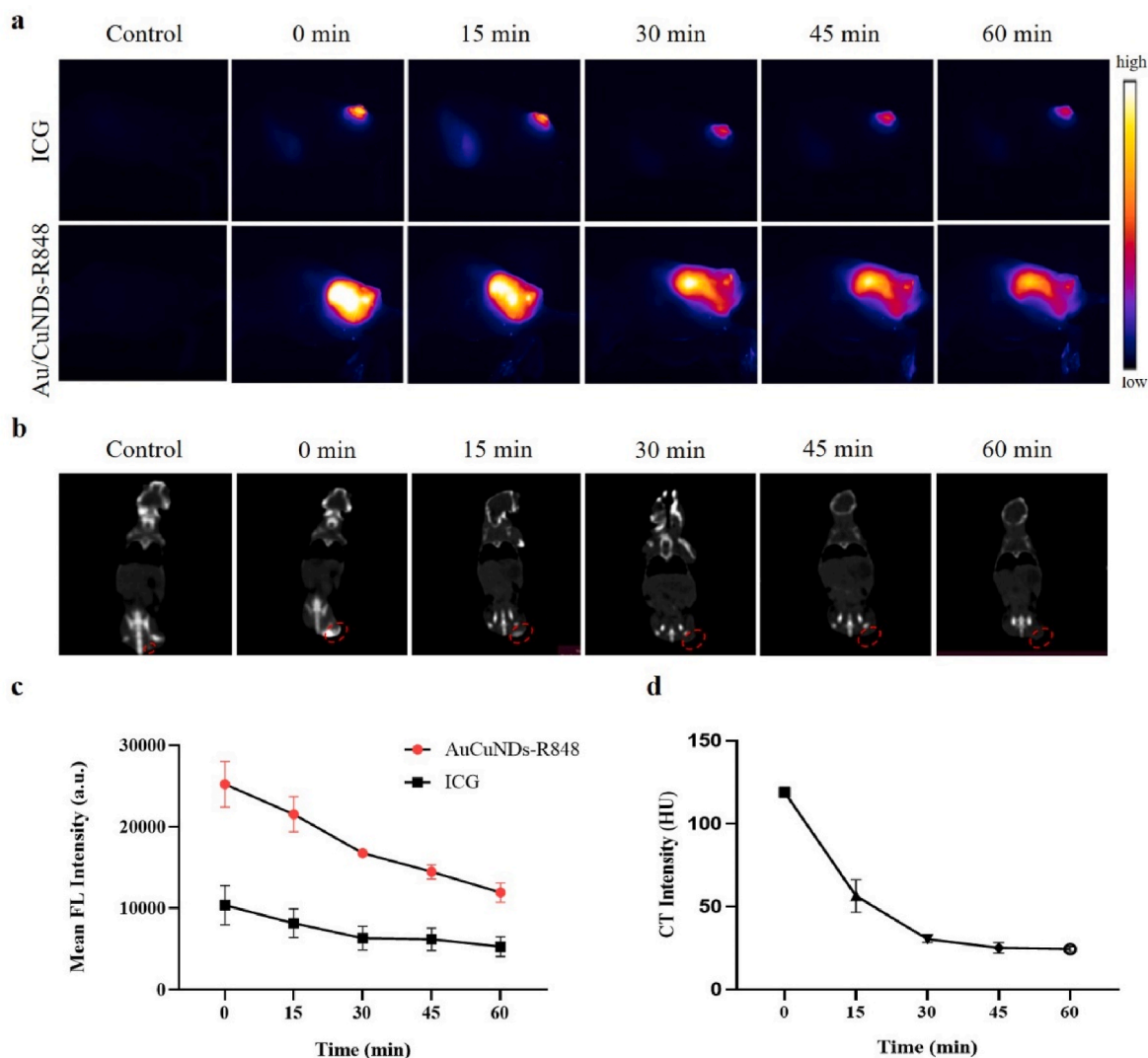


Fig. 6. *In vivo* NIR-II FL and CT imaging performance of Au/CuNDs-R848. (a) A comparative fluorescence imaging analysis between ICG and Au/CuNDs-R848. (b) CT imaging showcasing the capabilities of Au/CuNDs-R848. The red dashed box in each panel highlights the location of the tumor. (c) Quantitative evaluation based on the NIR-II fluorescence imaging data for ICG and Au/CuNDs-R848. (d) Trend analysis of CT intensity over time following the administration of Au/CuNDs-R848.

imaging-guided surgery is currently hampered by the lack of suitable fluorescent probes. The superior fluorescence imaging capabilities of Au/CuNDs-R848 provide a promising solution. We conducted an evaluation of the application of Au/CuNDs-R848 in surgical resection, guided by NIR-II fluorescence imaging. Upon administration of Au/CuNDs-R848, we observed an immediate and complete delineation of the entire tumor. Under the guidance of fluorescence imaging, the tumor was successfully excised in its entirety (Fig. S9). These findings strongly suggested that Au/CuNDs-R848 holds substantial promise for clinical applications.

2.8. *In vivo* induction of DAMPs

The *in vivo* release of DAMPs is essential for AuCuNDs-R848 to function as an “*in situ* nanovaccine”. We proceeded to evaluate the induction effect of Au/CuNDs-R848-mediated PTT/CDT synergistic therapy *in vivo*. Herein, we developed a bilateral TNBC mouse model, as illustrated in Fig. 7a. Primary tumors were initially established via subcutaneous injection of 4T1 cells into the left flank, with subsequent tumor cell injections into the right flank after 6 days to form distant tumors. During subsequent treatment, these distant tumors were

considered as “metastatic tumors” to evaluate the therapeutic efficacy of the designed “*in situ* nanovaccine” against metastatic TNBC. Once the primary tumors reached a volume of 80 mm³ on day 6 post-inoculation, the mice were randomly divided into six treatment groups (PBS, NIR, Au/CuNDs, Au/CuNDs+NIR, Au/CuNDs-R848, and Au/CuNDs-R848+NIR). All treatment protocols were administered according to the designated schedule, and no significant differences in body weights were observed among the groups (Fig. S10).

Then, the mice were euthanized, and the primary tumors were collected for further analysis. As depicted in Fig. 7b, ATP levels within primary tumors treated with Au/CuNDs-R848+NIR significantly increased, reaching 1.74 times those in the control group. This notable elevation facilitates the release of “find me” signal for dendritic cell precursors *in vivo*. Meanwhile, the expression of HMGB1 significantly increased upon Au/CuNDs-R848+NIR treatment (Fig. 7c). CLSM revealed a substantial HMGB1 translocation from nucleus to cytoplasm following Au/CuNDs-R848+NIR treatment, indicating the release of HMGB1 (Fig. 7d). HMGB1, either alone or in synergy with ATP, can stimulate efficient processing and cross-presentation of TAAs from dying cells by binding to toll-like receptor 4 (TLR4) on DCs [41]. Additionally, we observed an increase in CRT expression on the cell membrane of

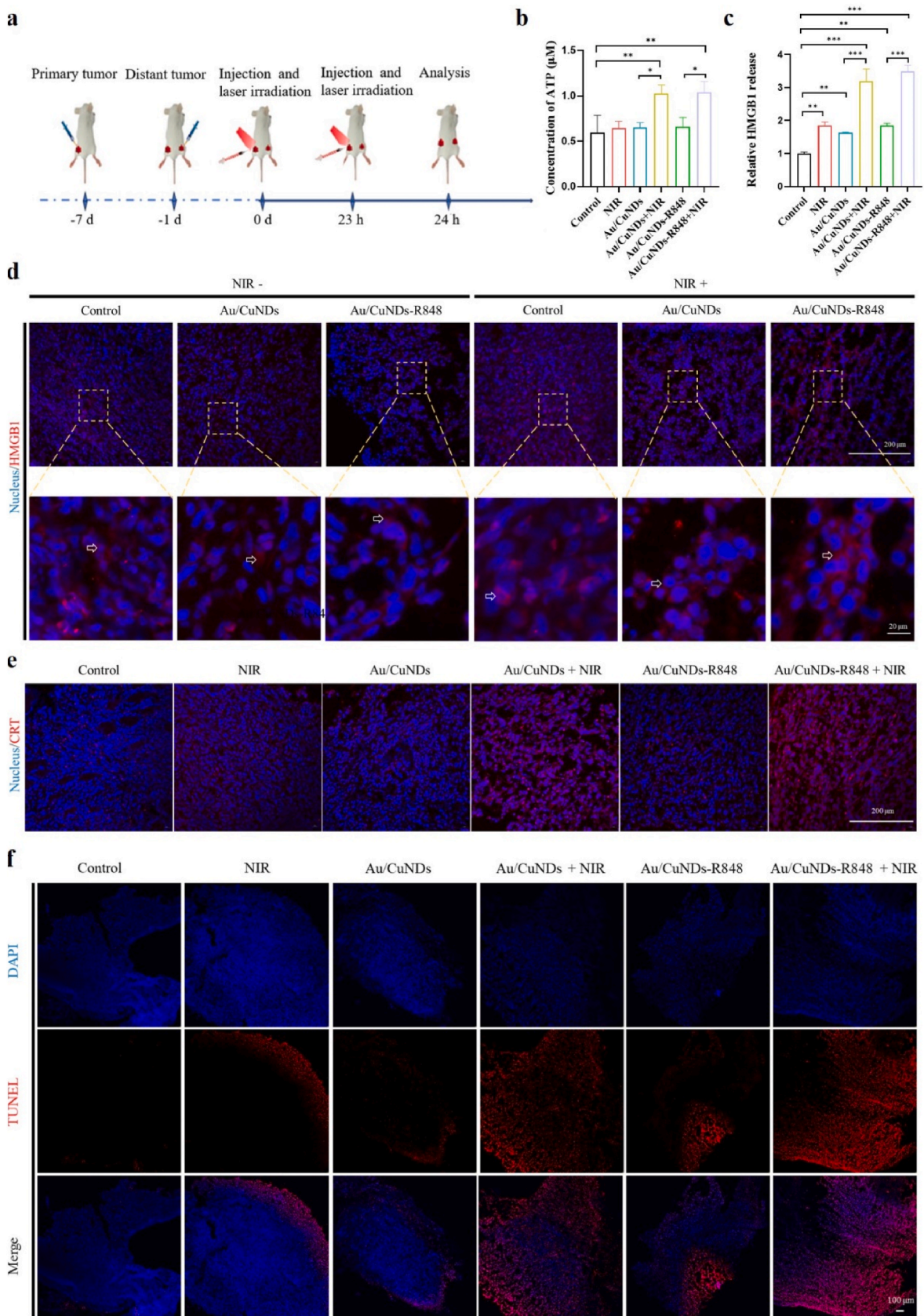


Fig. 7. *In vivo* induction of DAMPs by Au/CuNDs-R848-mediated PTT/CDT. (a) Scheme of the strategies employed to detect the release of DAMPs in mice bearing bilateral 4T1 tumors. (b) Measurement of extracellular ATP levels in the primary tumors. (c) Quantification of HMGB1 in the primary tumors as detected by ELISA. (d) Localization of HMGB1 in the primary tumors using CLSM, with cell nuclei counterstained with DAPI (blue). (scale bar: top, 200 μm ; bottom, 20 μm). (e) Evaluation of cell surface CRT (red) using CLSM. (scale bar: 200 μm). (f) TUNEL staining (red) of the primary tumors to identify apoptotic cells (scale bar: 100 μm) ($n = 6$). * $P < 0.05$, ** $P < 0.01$, *** $P < 0.001$.

primary tumors after different treatments. The increase in CRT expression was significantly amplified when treated with Au/CuNDs-R848+NIR (Fig. 7e). Collectively, these findings suggested that Au/CuNDs-R848+NIR treatment effectively induced the secretion of DAMPs *in vivo*.

Given that apoptosis is the main trigger for ICD, we performed TUNEL staining (a hallmark of apoptosis) on tumor sections to detect nuclear DNA fragmentation. As demonstrated in Fig. 7f, apoptosis was notably increased in the NIR, Au/CuNDs, Au/CuNDs-R848, Au/CuNDs+NIR, and Au/CuNDs-R848+NIR groups. In particular, the Au/CuNDs-R848+NIR group exhibited the most extensive apoptosis in primary tumors. These results strongly suggested that Au/CuNDs-R848+NIR treatment effectively induces apoptosis, leading to increased production of DAMPs via PTT and photothermal-enhanced CDT in primary tumors.

2.9. Optimization of treatment modalities

The high metastasis rate of TNBC often leads to occult metastases throughout the body, rendering limited effectiveness of many treatment modalities. Currently, the primary objective in managing metastases in TNBC is to alleviate symptoms and slow disease progression [42]. Although tumor vaccines represent a promising approach, their efficacy in preclinical trials is frequently constrained by technological limitations and inefficient vaccination cascade. In light of these challenges, an “*in situ* nanovaccine” Au/CuNDs-R848 was designed for imaging-guided PTT/CDT synergistic therapy to trigger dual immunoregulatory effects on TNBC.

Following the identification of tumor location via dual-mode *in vivo* imaging, mice were irradiated precisely after the injection of the nanomaterials. We studied the *in vivo* photothermal behavior of Au/CuNDs-R848, with temperature fluctuations monitored in real-time using an infrared thermal imaging camera. The results revealed that Au/CuNDs-R848 demonstrated exceptional *in vivo* photothermal properties, raising the temperature of the localized tumor to 55 °C upon laser irradiation ($\Delta T = 18$ °C), a level sufficient for tumor cell ablation (Fig. 8a). Through the combination of PTT and photothermal-enhanced CDT, Au/CuNDs-R848 is expected to achieve a favorable therapeutic effect on primary tumors and accomplish our objective in designing an “*in situ* nanovaccine”.

As reported, the successful development of an *in situ* vaccine necessitates a sequential cascade of events to effectively activate the immune system [43]. To optimize the effectiveness of immunotherapy, the implementation of a rational treatment modality is essential [44]. Therefore, it is crucial to determine the optimal treatment mode of the designed *in situ* vaccine. In light of this, we conducted an investigation to evaluate the therapeutic efficacy and immune activation capability of Au/CuNDs-R848 under different treatment modes. As depicted in Fig. S11a and b, we implemented different treatment schedules for mice bearing bilateral 4T1 tumors. Specifically, the mice underwent 4 cycles of treatment in different modes, including daily or alternate-day treatments of Au/CuNDs-R848 with laser irradiation. As indicated in Fig. S12, no significant differences in body weight were observed among the groups, showing the excellent *in vivo* biocompatibility of Au/CuNDs-R848 regardless of the treatment mode.

Eight days after different treatment modes, all mice were euthanized for further analysis, and photographs of both primary and distant tumors were captured (Fig. S13a and Fig. S15a). The results revealed that Au/CuNDs-R848 with laser irradiation significantly inhibited the growth of primary tumors, regardless of whether the treatment mode was daily or alternate days (Fig. S13b). Daily treatment with Au/CuNDs-R848 and laser irradiation potentially enabled complete ablation of primary tumors (Fig. S13). Importantly, daily treatment with Au/CuNDs-R848 and laser irradiation also significantly inhibited distant tumor growth (Fig. S14 and Fig. S15). Compared to alternate-day treatments, daily treatment exerted a relatively stronger inhibitory effect on both primary

and distant tumor growth. Moreover, daily treatment with Au/CuNDs-R848 and laser irradiation resulted in an elevation of plasma TNF- α levels (Fig. S16), a key pro-inflammatory factor known to exert tumor-suppressive effects. These findings indicate that daily treatment mode with Au/CuNDs-R848 and laser irradiation was more favorable for enhancing the efficacy of the “*in situ* nanovaccine”.

The additional results pertaining to the systemic immune response further corroborated the advantages of daily treatment with Au/CuNDs-R848. We collected spleens and distant tumors from both the daily and alternate-day treatment groups, followed by flow cytometry analysis according to the strategy outlined in Fig. S17. As shown in Fig. S18, daily treatment with Au/CuNDs-R848 and laser irradiation tended to enhance the maturation of DCs in the spleen, an effect not observed in the alternate-day treatment group. The maturation of DCs can effectively induce cytotoxic T lymphocytes infiltration, and as expected, the number of CD8⁺ T cells significantly increased following daily treatment with Au/CuNDs-R848 and laser irradiation (Fig. S19). Meanwhile, the number of CD4⁺ T cells also tended to increase with daily treatment (Fig. S20), representing one facet of dual immune regulation. Interestingly, as an important component of immunosuppressive cells, the number of MDSCs significantly decreased in both the spleen (Fig. S21) and distant tumors (Fig. S22) following daily treatment with Au/CuNDs-R848 and laser irradiation, constituting the other facet of dual immune regulation. Collectively, the above results revealed that daily treatment with Au/CuNDs-R848 exerted more potent dual immunomodulatory effects compared to alternate-day treatment, leading to enhanced immune activation and reversal of the immunosuppressive microenvironment. Therefore, daily treatment mode offered a more promising strategy for the success of the “*in situ* nanovaccine”.

2.10. *In vivo* anti-tumor effects

Having determined the optimal treatment mode of Au/CuNDs-R848, we proceeded to explore the immunotherapeutic effect and the underlying mechanisms *in vivo*. We conducted an *in vivo* experiment following the schedule outlined in Fig. 8b. Specifically, mice bearing tumors underwent daily treatments for 4 consecutive days with PBS, NIR, Au/CuNDs, Au/CuNDs+NIR, Au/CuNDs-R848, or Au/CuNDs-R848+NIR. Eight days after treatment, all mice were euthanized. Then, primary tumors, distant tumors, as well as vital organs (heart, liver, spleen, lung, and kidney) were collected for subsequent analysis.

We firstly assessed the efficacy of various treatment groups on both primary and distant tumors. For primary tumors, the NIR, Au/CuNDs, and Au/CuNDs-R848 groups exhibited slight inhibitory effects, indicating the limited effect of PTT and CDT alone. As expected, the Au/CuNDs + NIR and Au/CuNDs-R848+NIR groups significantly inhibited primary tumor growth (Fig. 8c, d and e). Importantly, the Au/CuNDs-R848+NIR group demonstrated superior tumor inhibition when compared to the Au/CuNDs+NIR group. The enhanced efficacy of Au/CuNDs-R848+NIR group could be attributed to the more efficient activation of systemic immunity. In the case of distant tumors, the Au/CuNDs-R848+NIR group displayed superior therapeutic effects when compared to other treatment groups. As illustrated in Fig. 8f, g, and h, the NIR, Au/CuNDs, and Au/CuNDs-R848 groups exhibited minimal inhibitory effects on distant tumor growth. Notably, the Au/CuNDs+NIR and Au/CuNDs-R848+NIR groups remarkably impeded the growth of distant tumors. Most significantly, the Au/CuNDs-R848+NIR group, benefiting from the combination of PTT, CDT, and R848, demonstrated a stronger ability to restrict the growth of distant tumors. All the above results revealed that Au/CuNDs-R848-mediated PTT/CDT had an outstanding therapeutic effect on both primary and distant tumors.

Furthermore, we analyzed immunostimulatory cytokines, including IL-6, IFN- γ , and TNF- α , to evaluate the antitumor immune response. Peripheral blood samples after treatment were collected to assess the levels of IL-6, IFN- γ , and TNF- α . The results were shown in Fig. 8i, j, and

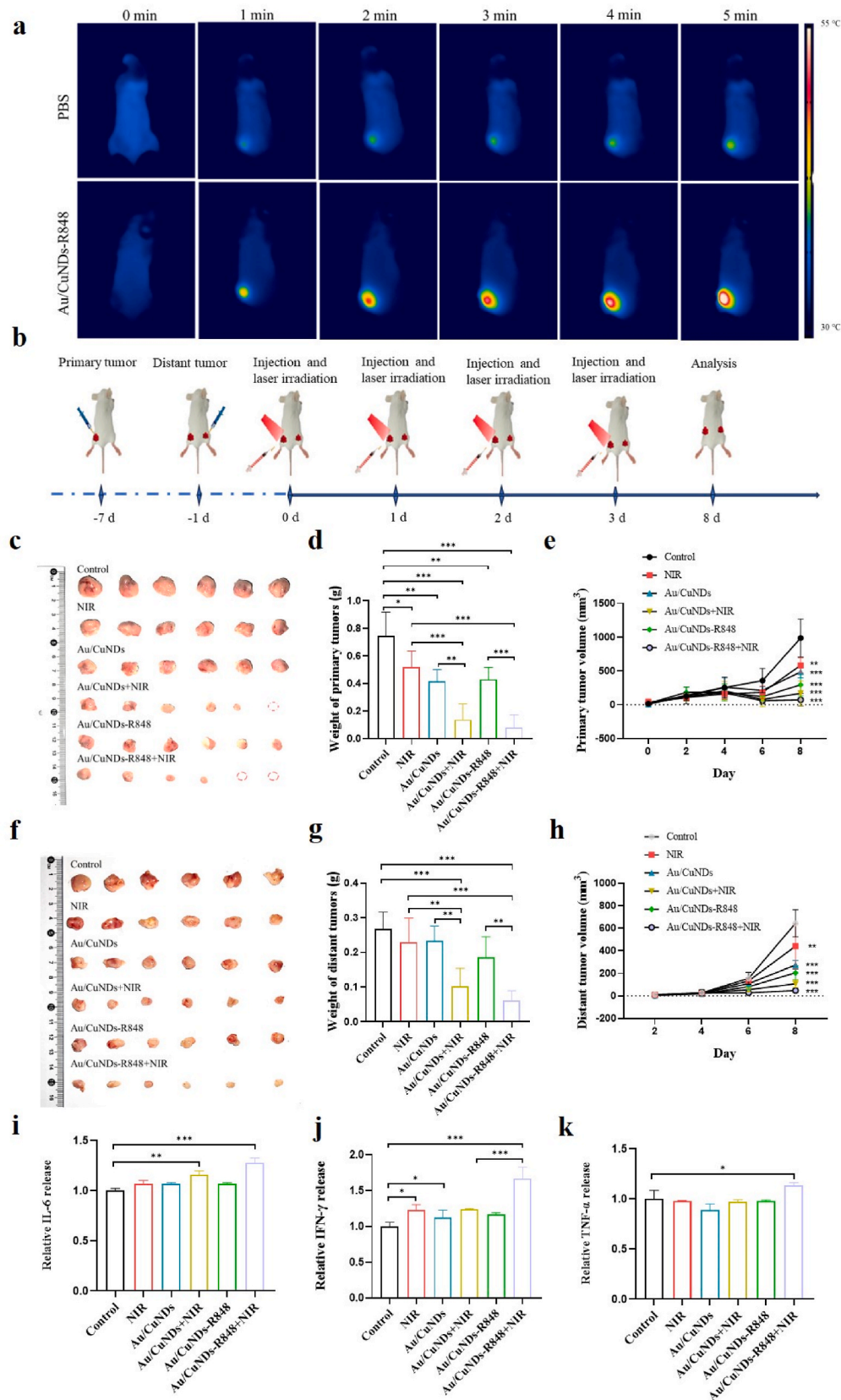


Fig. 8. *In vivo* treatment of primary and metastatic TNBC. (a) *In vivo* temperature changes under laser irradiation. (b) Treatment schedule for mice with bilateral 4T1 tumors. (c) Photographs, (d) weights, and (e) growth curves of primary tumors. (f) Photographs, (g) weights, and (h) growth curves of distant tumors. Plasma levels of (i) IL-6, (j) IFN- γ , and (k) TNF- α determined by ELISA (n = 6). * P < 0.05, ** P < 0.01, *** P < 0.001.

k. Remarkably, the levels of IL-6, IFN- γ , and TNF- α in the tumors of the Au/CuNDs-R848+NIR group were significantly higher compared to the other groups, exhibiting a 1.28-fold, 1.67-fold, and 1.13-fold increase, respectively, compared to the control group. These results highlighted the significant therapeutic potential of Au/CuNDs-R848 in the treatment of both primary and distant TNBC. Au/CuNDs-R848, in combination with laser irradiation, effectively modulated the immune response through harnessing the synergistic effects of PTT, photothermal-enhanced CDT, and the immunoadjuvant R848. In addition, throughout the experimental period, there were no significant changes in body weight across all treatment groups, as indicated in Fig. S23. Histopathological staining of collected organs revealed no substantial abnormalities (Fig. S24), further supporting the excellent *in vivo* biocompatibility of Au/CuNDs and Au/CuNDs-R848.

2.11. Mechanisms of enhanced immunotherapy

Achieving therapeutic efficacy of metastatic tumors necessitates systemic immune activation or the reversal of the immunosuppressive microenvironment. To delve deeper into the mechanisms of Au/CuNDs-R848-mediated PTT/CDT on the immune microenvironment, we collected distant tumors and spleens 8 days after treatment. These tissues were digested into single cells for flow cytometry analysis that focused on DCs, T lymphocytes, and MDSCs. In the spleen of tumor-bearing mice, there was a significant increase in mature DCs following treatment with Au/CuNDs-R848+NIR, as depicted in Fig. 9a and b. The recruitment and activation of DCs can facilitate the subsequent activation of T lymphocytes. Furthermore, in the spleen, compared to the control group, the ratio of CD3⁺ CD4⁺ cells (Fig. 9c and e) and CD3⁺ CD8⁺ cells (Fig. 9c and d) within CD45⁺ cell population significantly increased following treatment with Au/CuNDs-R848 and laser irradiation. CD8⁺ cytotoxic T lymphocytes can recognize the antigenic targets presented on tumors and subsequently secrete cytokines to eliminate tumor cells. Meanwhile, helper CD4⁺ T cells play an equally important role in the immune response by preventing CD8⁺ cytotoxic T lymphocytes exhaustion and maintaining the cytolytic responses of CTLs [45]. These results suggested that Au/CuNDs-R848-mediated PTT/CDT can effectively stimulate *in vivo* anti-tumor T cell immunity. Simultaneously, an increase in MDSCs within the immune microenvironment can suppress the anti-tumor immune response. Then, the ratio of MDSCs was measured. As shown in Fig. 9c and f, compared to the control group (21.45 \pm 2.9%), the ratio of CD11b⁺ Gr1⁺ MDSCs in the Au/CuNDs-R848 group decreased remarkably (7.22 \pm 3.96%), indicating a substantial and pronounced reversal of the immunosuppressive microenvironment.

To gain a deeper understanding of the regulatory effects of Au/CuNDs-R848-mediated PTT/CDT on the immune microenvironment, we conducted a comprehensive analysis of immune cell dynamics within the distant tumors. Notably, our findings demonstrated that the ratio of CD3⁺ CD4⁺ cells (Fig. 9g and h) and CD3⁺ CD8⁺ cells (Fig. 9g and i) within CD45⁺ cell population reached 18.78 \pm 4.63% and 13.65 \pm 7.54%, respectively, under the treatment of Au/CuNDs-R848 with laser irradiation. These results represented a significant increase compared with the control group. Meanwhile, the ratio of CD11b⁺ Gr1⁺ MDSCs significantly decreased following treatment with Au/CuNDs-R848 and laser irradiation (Fig. 9g and j). These results suggested that, apart from enhancing immune activation, Au/CuNDs-R848 with laser irradiation had the potential to reverse the immunosuppressive microenvironment. Ultimately, the “cold tumor” was transformed into a “hot tumor”, demonstrating the achievement of the “turning foes to friends” therapeutic strategy. All the above results collectively elucidated the mechanisms of exceptional therapeutic efficacy of Au/CuNDs-R848 with laser irradiation in treating distant tumors. Overall, the synthesized “*in situ* nanovaccine” can effectively regulate the immune microenvironment by enhancing immune activation and reversing the immunosuppressive microenvironment. This dual immunoregulatory approach holds great

promise for the treatment of both primary and metastatic TNBC, providing an innovative strategy for immunotherapy in the context of metastatic TNBC.

3. Conclusion

In summary, we have successfully developed “*in situ* nanovaccine” Au/CuNDs-R848 for dual-mode imaging-guided PTT and photothermal-enhanced CDT to enhance immunotherapy in both primary and metastatic TNBC. As a promising photothermal agent and nanozyme, the utilization of Au/CuNDs-R848 enabled synergistic PTT/CDT, effectively inhibiting the growth of primary tumors. Furthermore, the release of “individual” TAAs and DAMPs from primary tumors promoted the maturation of DCs and the infiltration of T lymphocytes, leading to the stimulation of a systemic anti-tumor immune response. Meanwhile, the myeloid-derived suppressor cells (MDSCs) were suppressed, thereby reversing the immunosuppressive microenvironment. Consequently, our approach triggered dual immunoregulatory effects and transformed the “cold tumor” into a “hot tumor” with an enhanced immune response, providing a compelling strategy of “turning foes to friends”. In addition, Au/CuNDs-R848 as a nanoprobe exhibited satisfactory dual-mode imaging performance, demonstrating its potential applications in clinical tumor detection and surgical guidance. Overall, the designed “*in situ* nanovaccine” effectively combines PTT, photothermal-enhanced CDT, and immunoadjuvant R848 to enhance immune response and sensitize tumor cells to ICD-based immunotherapy, providing a novel strategy for future immunotherapy.

4. Experimental section

4.1. Materials

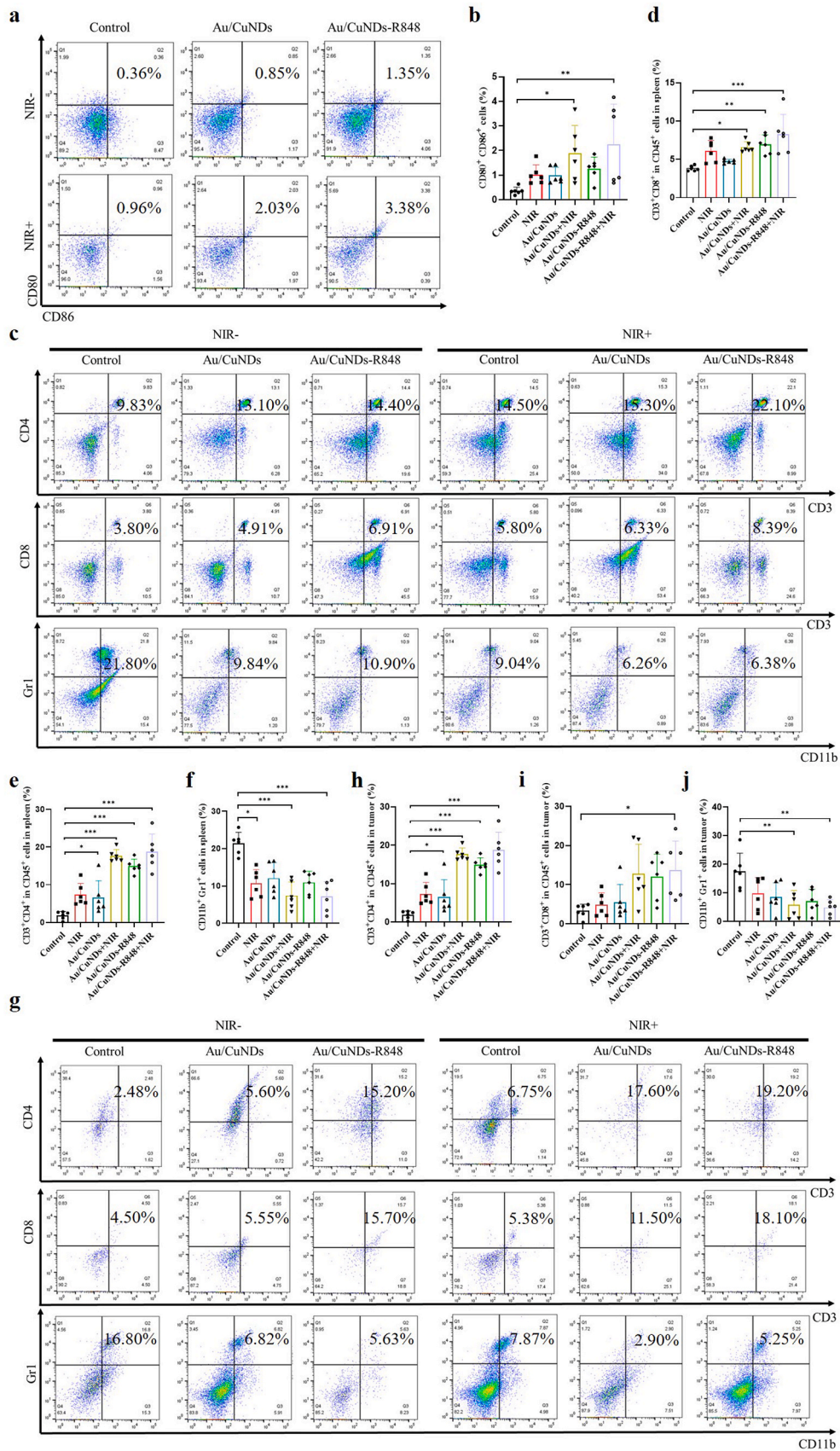
Tetrachloroauric (III) acid (HAuCl₄), 3-Mercaptopropionic acid (MPA), and branched polyethylene imine (PEI) were purchased from Sigma-Aldrich. Copper chloride (CuCl₂) and N, N-dimethylformamide (DMF) were purchased from Beijing Chemical Plant. Hydrazide hydrate (N₂H₄•H₂O), acetone, and chloroform were purchased from Sinopharm Chemical Reagent Co., Ltd. N-(3-dimethylaminopropyl)-N-ethylcarbodiimide hydrochloride (EDC) and N-hydroxysuccinimide (NHS) were purchased from Aladdin. R848 was purchased from MedChemExpress. All water used in the experiments was deionized.

4.2. Synthesis of ligand (SH-PEI)

First, 38 mg NHS and 64 mg EDC were dissolved in 40 mL DMF, followed by the addition of 300 μ L MPA while stirring continuously for 30 min. Next, 0.6 g PEI was dissolved in 2 mL ethanol and slowly added to the reaction mixture. The whole system was allowed to react at room temperature for 48 h under N₂ atmosphere. The product was then concentrated to 3 mL using vacuum distillation, after which a certain amount of acetone and chloroform were added. Following centrifugation at 8800 rpm for 15 min, the supernatant was removed. The precipitate was redissolved in 3 mL of water to obtain the ligand SH-PEI, which was stored at 4 °C for future use.

4.3. Synthesis of Au/CuNDs-R848

To a round-bottomed flask, 5 mL H₂O, 200 μ L SH-PEI, 250 μ L HAuCl₄ solution (50 mM), and 50 μ L CuCl₂ solution (50 mM) were added. Subsequently, 300 μ L N₂H₄•H₂O was added as a reducing agent. The mixture was maintained at 80 °C and stirred continuously for 4 h to obtain the Au/CuNDs. Following this, 2 mL Au/CuNDs and 100 μ L R848 solution were mixed and stirred at room temperature for 2 h. The obtained product was dialyzed in deionized water for 8 h, and Au/CuNDs-R848 solution was obtained.



(caption on next page)

Fig. 9. *In vivo* immune regulatory effects of Au/CuNDs-R848-mediated PTT/CDT against TNBC. (a) Flow cytometry analysis of the maturation of DCs. (b) Relative quantification of the maturation of DCs. (c) Flow cytometry analysis of CD8⁺ T cells (CD3⁺ and CD8⁺), CD4⁺ T cells (CD3⁺ and CD4⁺), and MDSCs (CD11b⁺ and Gr1⁺) in the spleen. (d) Relative quantification of CD8⁺ T cells, (e) CD4⁺ T cells, and (f) MDSCs in the spleen. (g) Flow cytometry analysis of CD8⁺ T cells (CD3⁺ and CD8⁺), CD4⁺ T cells (CD3⁺ and CD4⁺), and MDSCs (CD11b⁺ and Gr1⁺) in distant tumors. (h) Relative quantification of CD8⁺ T cells, (i) CD4⁺ T cells, and (j) MDSCs in distant tumors (n = 6). *P < 0.05, **P < 0.01, ***P < 0.001.

4.4. Characterization

¹H NMR measurements were performed using a Zhongke-Niujin Quantum-I NMR (400 MHz) spectrometer. Fourier transform infrared (FTIR) spectroscopy was performed by a Nicolet Avatar 360 FTIR spectrophotometer. The morphology of Au/CuNDs-R848 was examined using a JEOL TECNAI F20 transmission electron microscope. The UV–visible absorption spectra were carried out using a Lambda 800 UV–visible spectrophotometer. Zeta was determined by dynamic light scattering (DLS) using a Zetasizer Nano ZS particle size analyzer. X-ray photoelectron spectroscopy of Au/CuNDs-R848 was measured by a VG ESCALAB MKII spectrometer. The NIR-II fluorescence spectrum of Au/CuNDs-R848 was captured using an Edinburgh instrument FLS920 fluorescence spectrophotometer. The infrared thermal images were monitored using an infrared thermal imaging camera (FLIR T420).

4.5. ·OH generation induced by Au/CuNDs-R848

Methylene blue (MB) was used to test the production of ·OH. 2 mL Au/CuNDs-R848 solution, MB solution (100 µg/mL), and H₂O₂ solution (20, 40 and 60 mM) were added in sequence, and their UV–vis absorption spectra at 500 nm–800 nm were measured. Next, under different pH conditions (pH = 5.4, pH = 6.5 and pH = 7.4), 2 mL Au/CuNDs-R848 solution, 100 µg/mL MB solution and H₂O₂ aqueous solution were added in sequence, and their UV–vis absorption spectra at 500 nm–800 nm were measured. Finally, under different laser power densities (0.5, 1.0, 1.5, 2.0 W/cm²), 2 mL Au/CuNDs-R848 solution, 100 µg/mL MB solution and H₂O₂ aqueous solution were added in sequence, and their UV–vis absorption spectra at 500 nm–750 nm were measured.

The generation of ·OH radical was further confirmed by electron spin resonance (ESR) spectroscopy. Using 5,5'-dimethylpyrroline-1-oxide (DMPO) as spin trapping agent, the ·OH radical generated by Au/CuNDs-R848 in the presence of H₂O₂ (with or without NIR) was tested. Reaction groups include: (1) Au/CuNDs-R848 (2 mL)+H₂O₂+DMPO (20 µL); (2) Au/CuNDs-R848 (2 mL)+H₂O₂+DMPO (20 µL)+NIR (808 nm, 2.0 W/cm²). The mixture was then transferred into a quartz capillary and measured on an E500 spectrometer (BRUKER).

4.6. Depletion of extracellular GSH

GSH (2.5 mg/mL), DTNB (5 mg/mL) and Au/CuNDs-R848 (1 mL) were treated for different times (0, 10, 20, 30, 40 and 50 min) or different pH conditions (pH = 5.4, pH = 6.5 and pH = 7.4) to determine the capacity of GSH depletion. The consumption of GSH was measured by UV–vis spectrophotometer.

4.7. Cell lines

The HC11 cell line, a murine mammary epithelial cell line, was obtained from the Hospital of Stomatology, Jilin University. The 4T1 cell line, a murine triple-negative breast cancer cell line, was obtained from Haixing Bioscience (Suzhou, China). Both 4T1 and HC11 cell lines were cultured in RPMI-1640 medium (Gibco), supplemented with 10% fetal bovine serum (FBS, Clark Bioscience, Shanghai, China) and 1% penicillin/streptomycin (Hyclone). The cells were cultured at 37 °C in a humidified environment containing 5 % CO₂.

4.8. In vitro cytotoxicity assessment

4T1 and HC11 cells were seeded in 96-well plates at a density of 1 × 10⁴ cells per well and allowed to adhere overnight. The medium was then replaced with fresh medium containing varying concentrations of Au/CuNDs-R848 (0, 50, 100, 200, 300, 400 µg/mL). After a 24-h incubation, 10 µL of CCK-8 (Invigentech, USA) was added to each well, and the cells were incubated for an additional hour at 37 °C. The absorbance at 450 nm was detected using a versatile microplate detection system (Synergy™ HT, BioTek).

To evaluate the cytotoxicity of photothermal effect, 4T1 cells were treated with Au/CuNDs-R848 (200 µg/mL) and exposed to 808 nm laser irradiation at varying power densities (0, 1, 1.5, 2 W/cm²) for 5 min. After 24 h, cell viability was assessed using the CCK-8 assay as described above. Relative cell viability was calculated using the formula: (OD_{sample}-OD_{blank})/(OD_{control}-OD_{blank}) × 100%. All experiments were independently repeated 3 times.

4.9. Assessment of intracellular ROS generation

4T1 cells were seeded at a density of 1 × 10⁵ cells/well in 24-well plates and allowed to adhere overnight. The cells were then treated with Au/CuNDs-R848 (200 µg/mL) for 4 h, followed by laser irradiation at various power densities (0, 1, 1.5, 2 W/cm²) for 5 min. After washing with RPMI-1640 medium, the cells were incubated with 10 µmol DCFH-DA (Beyotime Biotechnology, China) in the dark at 37 °C for 20 min. The cells were then washed 3 times with RPMI-1640 medium, and fluorescence images were captured using an Olympus microscope (Japan) and analyzed with Image J software. The experiment was independently repeated 3 times.

4.10. Hemolysis assay

Fresh murine blood from female C57BL/6 mice was centrifuged at 1000 rpm for 10 min, and the erythrocytes were purified through 5 successive washes with PBS buffer. A 10 µL aliquot of the erythrocyte suspension was then mixed with 90 µL PBS, resulting in final concentrations of Au/CuNDs-R848 at varying levels (0, 50, 100, 200, 300, 400 µg/mL). Double deionized water (DDW) and PBS served as positive and negative controls, respectively. After a 2-h incubation at room temperature, the samples were centrifuged at 10,000 rpm for 3 min, and the absorbance of the supernatants at 540 nm was measured using a versatile microplate detection system (Synergy™ HT, BioTek). The percentage of hemolysis was calculated using the formula: (OD_{sample}-OD_{PBS})/(OD_{DDW}-OD_{PBS}) × 100%. The experiment was independently repeated 3 times.

4.11. In vitro cell apoptosis assay and live/dead cell staining

Cell apoptosis was assessed using an Annexin V-FITC (7AAD) Apoptosis Analysis Kit (Tianjin Simu Biotech Co., Ltd) according to the manufacturer's instructions. Briefly, 4T1 cells were seeded at a density of 1 × 10⁵ cells per well in 24-well plates and allowed to adhere overnight. The cells were then treated under various conditions (control, laser irradiation, Au/CuNDs, Au/CuNDs with laser irradiation, Au/CuNDs-R848, and Au/CuNDs-R848 with laser irradiation) for 24 h. Approximately 1 × 10⁶ cells were harvested, washed with cold PBS, and stained with 5 µL Annexin V-FITC and 5 µL 7-AAD for 25 min at room temperature in the dark. The stained cells were then immediately

analyzed by flow cytometry (MACSQuant® Analyzer, Germany), with all steps completed within 1 h.

In addition to the apoptosis assay, a Calcein/PI Cell Viability/Cytotoxicity Assay Kit (Beyotime Biotechnology, China) was used according to the manufacturer's instructions. The 4T1 cells were treated as described above, and then stained with calcein AM and PI for 30 min at 37 °C in the dark. Finally, immunofluorescence images were captured using an Olympus microscope (Japan).

4.12. Detection of CRT, HMGB1, and ATP

4T1 cells were seeded at a density of 1×10^5 cells per well in 24-well plates and incubated overnight. Cells were then subjected to various treatment conditions (control, laser irradiation, Au/CuNDs, Au/CuNDs with laser irradiation, Au/CuNDs-R848, and Au/CuNDs-R848 with laser irradiation) for a specific duration.

To detect CRT exposure, cells were collected after a 12-h treatment. The collected cells were then incubated with rabbit anti-calreticulin (1:100, bs-5913R, Bioss) for 30 min at 4 °C, followed by staining with fluorescein (FITC)-conjugated Affinipure Goat Anti-Rabbit IgG staining (1:200, SA00003-2, Proteintech) for 30 min and DAPI (D3571, Invitrogen) for 5 min at 4 °C. CRT exposure was measured by flow cytometry (MACSQuant® Analyzer, Germany), and the results were analyzed using FlowJo V10.8.1 software.

To detect HMGB1, the cell culture supernatant was collected after 24 h and analyzed using a mouse HMGB-1 ELISA Kit (Mlbio, China) according to the manufacturer's instructions. Additionally, immunofluorescent staining was performed to examine the cellular localization of HMGB1. Specifically, 4T1 cells were fixed with 4 % paraformaldehyde and permeabilized with Triton X-100. The cells were then incubated with primary anti-HMGB1 antibodies (1:1000, ab18256, Abcam) overnight at 4 °C, followed by incubation with CoraLite594-conjugated Goat Anti-Rabbit IgG (1:200, SA00013-4, Proteintech) for 2 h and DAPI for 5 min at room temperature. HMGB1 release was detected using a Confocal Laser Scanning Microscope (CLSM).

To measure ATP levels, the cell culture supernatant was collected after 2 h, and ATP levels were measured using an Enhanced ATP Assay Kit (S0027, Beyotime) according to the manufacturer's instructions.

4.13. In vitro activation and maturation of BMDCs

BMDCs were generated from the bone marrow of 6-week-old C57BL/6 female mice and cultured in RPMI-1640 medium (Gibco) supplemented with 10% fetal bovine serum (FBS, Clark Bioscience, Shanghai, China) and 1 % penicillin/streptomycin (Hyclone). Recombinant murine GM-CSF (20 ng/mL, 315-03, PeproTech) and recombinant murine IL-4 (20 ng/mL, 214-14, PeproTech) were added to promote BMDCs differentiation and maturation. Half of the medium was replaced every other day, and cells harvested on day 6 were considered immature DCs.

For the co-culture experiments, 4T1 cells were seeded at a density of 1×10^5 cells per well in 24-well plates and pretreated with various treatment conditions (control, laser irradiation, Au/CuNDs, Au/CuNDs with laser irradiation, Au/CuNDs-R848, and Au/CuNDs-R848 with laser irradiation). Immature DCs were then co-cultured with the treated 4T1 cells for an additional 24 h. Lipopolysaccharide (LPS) (100 ng/mL, L2880, Sigma) served as the positive control.

To assess the maturation of BMDCs, cells were incubated with mouse Fc receptors (Miltenyi Biotec, Germany) for 10 min. Subsequently, the cells were stained with FITC anti-mouse CD11c (1:200, FITC-65130, Proteintech), APC anti-mouse CD86 (1:100, 105011, Biolegend), and PE anti-mouse CD80 (1:100, PE-65076, Proteintech). The maturation of BMDCs was assessed by flow cytometry (MACSQuant® Analyzer, Germany).

4.14. Primary and distant tumor models

Female C57BL/6 and Balb/c mice, aged 6 weeks and weighing 20 ± 2 g, were supplied by Changchun Yisi Experimental Animal Technology Co., Ltd., Changchun, China. Protocols involved in the use of animals were reviewed and approved by the Institutional Review Board and Institutional Animal Care and Use Committee of the First Hospital of Jilin University. All experiments were performed following the approved protocols (Approval No. 20220902-01).

To establish the primary 4T1 tumor model, we injected 1.5×10^6 4T1 cells (200 μ L) into the left flank of Balb/c mice. The distant 4T1 tumor model was established by injecting 1.2×10^6 4T1 cells (200 μ L) into the right flank of Balb/c mice after 6 days. All mice bearing 4T1 tumors were randomly divided into 6 groups: PBS treatment (100 μ L), PBS (100 μ L) with laser irradiation (2 W/cm², 5 min), Au/CuNDs treatment (10 mg/kg), Au/CuNDs (10 mg/kg) with laser irradiation (2 W/cm², 5 min), Au/CuNDs-R848 treatment (10 mg/kg), and Au/CuNDs-R848 (10 mg/kg) with laser irradiation (2 W/cm², 5 min) ($n = 6$ for each group).

4.15. In vivo detection of ICD

The treatments for the 6 groups were administered on days 7 and 8. After 24 h of the first treatment, the mice were sacrificed, and primary tumor tissues were collected for the preparation of frozen tissue sections and subsequent ATP and HMGB1 kit assays. The ATP and HMGB1 detection procedures were performed according to the manufacturer's standard protocols.

For immunofluorescence staining, the primary tumor tissues were fixed with 4 % paraformaldehyde and incubated with primary antibodies against CRT and HMGB1 overnight at 4 °C, followed by incubation with CoraLite594-conjugated goat anti-rabbit secondary antibody for 30 min at 37 °C. Nuclei were stained with DAPI at room temperature for 5 min. The sections were then washed and observed by CLSM. In addition, apoptosis in primary tumor tissues was assessed using a One Step TUNEL Apoptosis Assay Kit (C1089, Beyotime) according to the manufacturer's instructions.

4.16. In vivo FL and CT imaging

Female Balb/c mice bearing 4T1 tumors were selected for FL and CT imaging. Specifically, 10 mg/kg Au/CuNDs-R848 and 200 μ M ICG were intratumorally injected. Then the mice were subjected to two-dimensional FL imaging using a NIRvana-640 InGaAs camera (Princeton Instruments) at 0, 15, 30, 45, and 60 min. The fluorescence intensity was then evaluated. Finally, the mice were euthanized, and vital organs including the heart, liver, spleen, lung, and kidney, as well as the tumors, were dissected for fluorescence imaging.

For CT imaging, 10 mg/kg Au/CuNDs-R848 were intratumorally injected, and the mice were subjected to CT scans at 0, 15, 30, 45, and 60 min using a CT scanner system (United-Imaging, uCT 760). Then, quantitative analysis of the CT value was conducted.

4.17. In vivo imaging-guided surgical resection

Female Balb/c mice bearing 4T1 tumors were anesthetized and intratumorally injected with Au/CuNDs-R848 (10 mg/kg). Then, fluorescence imaging was conducted to visualize the tumor boundary. With FL imaging, the tumor was clearly demarcated and subsequently surgically resected.

4.18. Selection of treatment regimens

Balb/c mice bearing 4T1 tumors were divided into two treatment groups: PBS (100 μ L) and Au/CuNDs-R848 (10 mg/kg) with laser irradiation (2 W/cm², 5 min). The treatments were initiated on day 7 and

administered either daily or every other day for a total of 4 times ($n = 6$). On the 8th day after the first treatment, the mice were euthanized, and blood samples were collected to measure serum levels of TNF- α using an ELISA kit (Proteintech) according to the manufacturer's protocols. The primary and distant tumors were then collected for vol/wt measurements and flow cytometry analysis.

For flow cytometry analysis, the collected tumor tissues were stained with the following antibodies: FITC anti-mouse CD11c, APC anti-mouse CD86, PE anti-mouse CD80, APC anti-mouse CD45.2 (1:100, 109813, Biolegend), FITC anti-mouse CD3 ϵ (1:50, 100305, Biolegend), PE/Cyanine7 anti-mouse CD4 (1:100, 100421, Biolegend), PE/Cyanine5 anti-mouse CD8a (1:100, 100709, Biolegend), FITC anti-mouse/human CD11b (1:50, 101205, Biolegend), and PE anti-mouse Gr1 (1:100, 108407, Biolegend). Flow cytometry analysis was performed using a MACSQuant[®] Analyzer (Germany) to assess the maturation of DCs in the spleen, as well as the populations of intratumoral/intrasplenic T cells and MDSCs.

4.19. Anti-tumor study

Balb/c mice bearing 4T1 tumors were divided into the six aforementioned groups, and the treatments were administered daily starting on day 7 ($n = 6$). Tumor growth and mouse weight were monitored every 2 days. Blood samples were collected to measure serum levels of IL-6, TNF- α , and IFN- γ using ELISA kits (Proteintech) according to the manufacturer's protocols. The primary and distant tumors were collected for vol/wt measurements, as well as for subsequent flow cytometry analysis, as described previously.

4.20. Statistical analysis

Data are expressed as mean \pm SEM or mean \pm SD, and statistical analysis between groups was performed using GraphPad Prism 8. For data involving multiple groups, statistical significance was determined using one-way analysis of variance (ANOVA). For comparisons between two groups, unpaired two-tailed Student's *t*-tests were used.

Ethics approval and consent to participate

Protocols involved in the use of animals were reviewed and approved by the Institutional Review Board and Institutional Animal Care and Use Committee of the First Hospital of Jilin University. All experiments were performed following the approved protocols (Approval No. 20220902-01).

CRediT authorship contribution statement

Ze Wang: Writing – original draft, Validation, Software, Methodology, Investigation, Formal analysis, Data curation, Conceptualization. **Tong Sha:** Writing – original draft, Methodology, Investigation, Formal analysis, Conceptualization. **Jinwei Li:** Software, Methodology, Investigation, Data curation. **Huanyu Luo:** Software, Methodology, Investigation. **Annan Liu:** Writing – original draft, Software, Data curation. **Hao Liang:** Data curation, Conceptualization. **Jinbiao Qiang:** Software, Conceptualization. **Lei Li:** Methodology. **Andrew K. Whittaker:** Supervision. **Bai Yang:** Supervision. **Hongchen Sun:** Supervision. **Ce Shi:** Writing – review & editing, Validation, Supervision, Methodology, Funding acquisition, Data curation, Conceptualization. **Quan Lin:** Writing – review & editing, Supervision, Methodology, Funding acquisition, Formal analysis, Data curation, Conceptualization.

Declaration of competing interest

The authors declare no competing financial interest.

Acknowledgement

This work was supported by the National Key Research and Development Program of China (2022YFC2504200), the National Natural Science Foundation of China (Nos. 82270959 and 81970903), the Natural Science Foundation of Jilin Province (No. SKL202302002), the Key Research and Development Project of Jilin Provincial Science and Technology Department (Nos. 20210204142YY), the Jilin University Norman Bethune Program (No. 2023B28), the Fundamental Research Funds for the Central Universities, the Natural Science Foundation of Liaoning Province (No. 2022-BS-123), the Science and Technology Project of Shenyang (No. 21-173-9-34), and “Medical + X” Interdisciplinary Innovation Team “Announcement and Leadership” Construction Project (2022JBGS08).

Appendix A. Supplementary data

Supplementary data to this article can be found online at <https://doi.org/10.1016/j.bioactmat.2024.04.023>.

References

- [1] X.Q. Wang, E. Danenberg, C.S. Huang, D. Egle, M. Callari, B. Bermejo, et al., Spatial predictors of immunotherapy response in triple-negative breast cancer, *Nature* (2023).
- [2] X.T. Li, Z. Zhang, F.Y. Gao, Y.X. Ma, D.Y. Wei, Z.W. Lu, et al., c-Myc-Targeting PROTAC based on a TNA-DNA bivalent binder for combination therapy of triple-negative breast cancer, *J. Am. Chem. Soc.* 145 (2023) 9334–9342.
- [3] K.G.K. Deepak, R. Vempati, G.P. Nagaraju, V.R. Dasari, N. S. D.N. Rao, et al., Tumor microenvironment: challenges and opportunities in targeting metastasis of triple negative breast cancer, *Pharmacol. Res.* 153 (2020) 104683.
- [4] L. Yin, J.-J. Duan, X.-W. Bian, S.-C. Yu, Triple-negative breast cancer molecular subtyping and treatment progress, *Breast Cancer Res.* 22 (2020) 61.
- [5] N.S. Zhang, X.L. Liang, C. Gao, M. Chen, Y.M. Zhou, C.J. Krueger, et al., Loading lovastatin into camptothecin-floxuridine conjugate nanocapsules for enhancing anti-metastatic efficacy of cocktail chemotherapy on triple-negative breast cancer, *ACS Appl. Mater. Inter.* 10 (2018) 29385–29397.
- [6] Y. Wang, Y. Ding, D. Yao, H. Dong, C. Ji, J. Wu, et al., Copper-based nanoscale coordination polymers augmented tumor radioimmunotherapy for immunogenic cell death induction and T-cell infiltration, *Small* 17 (2021) e2006231.
- [7] P. Bao, Z.T. Zheng, J.J. Ye, X.Z. Zhang, Apoptotic body-mediated intracellular delivery strategy for enhanced STING activation and improved tumor immunogenicity, *Nano Lett.* 22 (2022) 2217–2227.
- [8] S. Kumar, D.W. Wilkes, N. Samuel, M.A. Blanco, A. Nayak, K. Alicea-Torres, et al., Δ Np63-driven recruitment of myeloid-derived suppressor cells promotes metastasis in triple-negative breast cancer, *J. Clin. Invest.* 128 (2018) 5095–5109.
- [9] B. Yu, F. Luo, B. Sun, W. Liu, Q. Shi, S.-Y. Cheng, et al., KAT6A acetylation of SMAD3 regulates myeloid-derived suppressor cell recruitment, metastasis, and immunotherapy in triple-negative breast cancer, *Adv. Sci.* 8 (2021) e2100014.
- [10] T. Yamazaki, D. Hannani, V. Poirier-Colame, S. Ladoire, C. Locher, A. Sistigu, et al., Defective immunogenic cell death of HMGB1-deficient tumors: compensatory therapy with TLR4 agonists, *Cell Death Differ.* 21 (2014) 69–78.
- [11] D.V. Krysko, A.D. Garg, A. Kaczmarek, O. Krysko, P. Agostinis, P. Vandenabeele, Immunogenic cell death and DAMPs in cancer therapy, *Nat. Rev. Cancer* 12 (2012) 860–875.
- [12] Z. Li, X. Lai, S. Fu, L. Ren, H. Cai, H. Zhang, et al., Immunogenic cell death activates the tumor immune microenvironment to boost the immunotherapy efficiency, *Adv. Sci.* 9 (2022) e2201734.
- [13] R. Alzeibak, T.A. Mishchenko, N.Y. Shilyagina, I.V. Balalaeva, M.V. Vedunova, D. V. Krysko, Targeting immunogenic cancer cell death by photodynamic therapy: past, present and future, *J. Immunother. Clin* 9 (2021).
- [14] Y. Wang, F. Gao, X. Li, G. Niu, Y. Yang, H. Li, et al., Tumor microenvironment-responsive fenton nanocatalysts for intensified anticancer treatment, *J. Nanobiotechnol.* 20 (2022) 69.
- [15] L. Wang, W. Jiang, Y. Su, M. Zhan, S. Peng, H. Liu, et al., Self-splittable transcytosis nanoraspberry for NIR-II photo-immunometabolic cancer therapy in deep tumor tissue, *Adv. Sci.* 9 (2022) e2204067.
- [16] Z. Wang, H.Y. Xing, A.N. Liu, L. Guan, X.C. Li, L. He, et al., Multifunctional nanosystem for multi-mode targeted imaging and enhanced photothermal therapy of metastatic prostate cancer, *Acta Biomater.* 166 (2023) 581–592.
- [17] Z. Wang, L. He, S.T. Che, H.Y. Xing, L. Guan, Z. Yang, et al., AuNCs-LHRHa nanosystem for FL/CT dual-mode imaging and photothermal therapy of targeted prostate cancer, *J. Mater. Chem. B* 10 (2022) 5182–5190.
- [18] T.X. Jin, D. Cheng, G.Y. Jiang, W.Q. Xing, P.W. Liu, B. Wang, et al., Engineering naphthalimide-cyanine integrated near-infrared dye into ROS-responsive nanohybrids for tumor PDT/PTT/chemotherapy, *Bioact. Mater.* 14 (2022) 42–51.
- [19] M.T. Niu, Q.W. Chen, Z. Chen, X.H. Liu, Q.X. Huang, J.L. Liang, et al., Immunoadjuvant-modified potentiate cancer photothermal immunotherapy, *Nano Lett.* 24 (2023) 130–139.

- [20] Q.L. Mao, J. Fang, A.N. Wang, Y.Q. Zhang, C.X. Cui, S.Y. Ye, et al., Aggregation of gold nanoparticles triggered by hydrogen peroxide-initiated chemiluminescence for activated tumor theranostics, *Angew. Chem., Int. Ed.* 60 (2021) 23805–23811.
- [21] Q.X. Zhong, J. Feng, B. Jiang, Y.L. Fan, Q. Zhang, J.X. Chen, et al., Strain-modulated seeded growth of highly branched black Au superparticles for efficient photothermal conversion, *J. Am. Chem. Soc.* 143 (2021) 20513–20523.
- [22] Y.-J. He, X.-Y. Liu, L. Xing, X. Wan, X. Chang, H.-L. Jiang, Fenton reaction-independent ferroptosis therapy via glutathione and iron redox couple sequentially triggered lipid peroxide generator, *Biomaterials* 241 (2020) 119911.
- [23] Y.M. Wang, D. Wang, Y.Y. Zhang, H. Xu, L.X. Shen, J. Cheng, et al., Tumor microenvironment-adaptive nanoplatform synergistically enhances cascaded chemodynamic therapy, *Bioact. Mater.* 22 (2023) 239–253.
- [24] T.T. Wang, H. Zhang, H.H. Liu, Q. Yuan, F. Ren, Y.B. Han, et al., Boosting H₂O₂-guided chemodynamic therapy of cancer by enhancing reaction kinetics through versatile biomimetic fenton nanocatalysts and the second near-infrared light irradiation, *Adv. Funct. Mater.* 30 (2020).
- [25] S.A. Polash, T. Khare, V. Kumar, R. Shukla, Prospects of exploring the metal-organic framework for combating antimicrobial resistance, *ACS Appl. Bio Mater.* 4 (2021) 8060–8079.
- [26] M. Wang, M.Y. Chang, C.X. Li, Q. Chen, Z.Y. Hou, B.G. Xing, et al., Tumor-microenvironment-activated reactive oxygen species amplifier for enzymatic cascade cancer starvation/chemodynamic/immunotherapy, *Adv. Mater.* 34 (2022).
- [27] L. An, C.B. Wang, Q.W. Tian, C. Tao, F.F. Xue, S.P. Yang, et al., NIR-II laser-mediated photo-Fenton-like reaction plasmonic Cu₉S₈ for immunotherapy enhancement, *Nano Today* 43 (2022).
- [28] L.J. Jin, D.M. Yang, Y.H. Song, D.D. Li, W.J. Xu, Y.Q. Zhu, et al., Programming of nanovaccines for lymph node-targeted delivery and cancer immunotherapy, *ACS Nano* (2022).
- [29] T. Li, G.J. Chen, Z.C. Xiao, B. Li, H.H. Zhong, M.Z. Lin, et al., Surgical tumor-derived photothermal nanovaccine for personalized cancer therapy and prevention, *Nano Lett.* 22 (2022) 3095–3103.
- [30] V. Mata-Haro, C. Cekic, M. Martin, P.M. Chilton, C.R. Casella, T.C. Mitchell, The vaccine adjuvant monophosphoryl lipid A as a TRIF-biased agonist of TLR4, *Science* 316 (2007) 1628–1632.
- [31] G. Kroemer, L. Galluzzi, O. Kepp, L. Zitvogel, Immunogenic cell death in cancer therapy, *Annu. Rev. Immunol.* 31 (2013) 51–72.
- [32] Q. Ni, F. Zhang, Y. Liu, Z. Wang, G. Yu, B. Liang, et al., A bi-adjuvant nanovaccine that potentiates immunogenicity of neoantigen for combination immunotherapy of colorectal cancer, *Sci. Adv.* 6 (2020) eaaw6071.
- [33] G.M. Lynn, P. Chytil, J.R. Francica, A. Lagová, G. Kueberuwa, A.S. Ishizuka, et al., Impact of polymer-TLR-7/8 agonist (adjuvant) morphology on the potency and mechanism of CD8 T cell induction, *Biomacromolecules* 20 (2019) 854–870.
- [34] P.-M. Chen, W.-Y. Pan, C.-Y. Wu, C.-Y. Yeh, C. Korupalli, P.-K. Luo, et al., Modulation of tumor microenvironment using a TLR-7/8 agonist-loaded nanoparticle system that exerts low-temperature hyperthermia and immunotherapy for *in situ* cancer vaccination, *Biomaterials* 230 (2020) 119629.
- [35] Z. Wang, X.L. Ou, L. Guan, X.C. Li, A.A. Liu, L. Li, et al., Pomegranate-inspired multifunctional nanocomposite wound dressing for intelligent self-monitoring and promoting diabetic wound healing, *Biosens. Bioelectron.* 235 (2023).
- [36] Z. Wang, D.Z. Wang, X.J. Ren, Z.S. Liu, A.N. Liu, X.C. Li, et al., One stone, three birds: multifunctional nanodots as “pilot light” for guiding surgery, enhanced radiotherapy, and brachytherapy of tumors, *ACS Central Sci.* 9 (2023) 1976–1988.
- [37] R.Z. Hu, Y. Fang, M.F. Huo, H.L. Yao, C.M. Wang, Y. Chen, et al., Ultrasmall Cu₂-XS nanodots as photothermal-enhanced Fenton nanocatalysts for synergistic tumor therapy at NIR-II biowindow, *Biomaterials* 206 (2019) 101–114.
- [38] M. Obeid, A. Tesniere, F. Ghiringhelli, G.M. Fimia, L. Apetoh, J.-L. Perfettini, et al., Calreticulin exposure dictates the immunogenicity of cancer cell death, *Nat. Med.* 13 (2007) 54–61.
- [39] J. Fucikova, O. Kepp, L. Kasikova, G. Petroni, T. Yamazaki, P. Liu, et al., Detection of immunogenic cell death and its relevance for cancer therapy, *Cell Death Dis.* 11 (2020) 1013.
- [40] J. Zhou, G. Wang, Y. Chen, H. Wang, Y. Hua, Z. Cai, Immunogenic cell death in cancer therapy: present and emerging inducers, *J. Cell Mol. Med.* 23 (2019) 4854–4865.
- [41] A. Ahmed, S.W.G. Tait, Targeting immunogenic cell death in cancer, *Mol. Oncol.* 14 (2020) 2994–3006.
- [42] S. Al-Mahmood, J. Sapiezynski, O.B. Garbuzenko, T. Minko, Metastatic and triple-negative breast cancer: challenges and treatment options, *Drug Deliv. Transl. Res.* 8 (2018) 1483–1507.
- [43] H. Locy, S. de Mey, W. de Mey, M. De Ridder, K. Thielemans, S.K. Maenhout, Immunomodulation of the tumor microenvironment: turn foe into friend, *Front. Immunol.* 9 (2018) 2909.
- [44] J. Ran, T. Liu, C. Song, Z. Wei, C. Tang, Z. Cao, et al., Rhythm mild-temperature photothermal therapy enhancing immunogenic cell death response in oral squamous cell carcinoma, *Adv. Healthcare Mater.* 12 (2023) e2202360.
- [45] C.-H. Ke, Y.-H. Chiu, K.-C. Huang, C.-S. Lin, Exposure of immunogenic tumor antigens in surrendered immunity and the significance of autologous tumor cell-based vaccination in precision medicine, *Int. J. Mol. Sci.* 24 (2022).